

The Young Outer Disk of M83 ¹

T. J. Davidge

*Herzberg Institute of Astrophysics,
National Research Council of Canada, 5071 West Saanich Road,
Victoria, BC Canada V9E 2E7
email: tim.davidge@nrc.ca*

ABSTRACT

Deep near-infrared images recorded with NICI on Gemini South are used to investigate the evolved stellar content in the outer regions of the south east quadrant of the spiral galaxy M83. A diffuse population of asymptotic giant branch (AGB) stars is detected, indicating that there are stars outside of the previously identified young and intermediate age star clusters in the outer disk. The brightest AGB stars have $M_K \geq -8$, and the AGB luminosity function (LF) is well-matched by model LFs that assume ages ≤ 1 Gyr. The specific SFR during the past few Gyr estimated from AGB star counts is consistent with that computed from mid-infrared observations of star clusters at similar radii, and it is concluded that the disruption timescale for star clusters in the outer disk is $\ll 1$ Gyr. The luminosity function and specific frequency of AGB stars varies with radius, in a manner that is indicative of lower luminosity-weighted ages at larger radii. Modest numbers of red supergiants (RSGs) are also found, indicating that there has been star formation during the past 100 Myr, while the ratio of C stars to M giants is consistent with that expected for a solar metallicity system that has experienced a constant star formation rate (SFR) for the past few Gyrs. The results drawn from the properties of resolved AGB stars are broadly consistent with those deduced from integrated light observations in the UV.

Subject headings: galaxies: individual M83 – galaxies: evolution – galaxies: spiral

¹Based on observations obtained at the Gemini Observatory, which is operated by the Association of Universities for Research in Astronomy, Inc., under a co-operative agreement with the NSF on behalf of the Gemini partnership: the National Science Foundation (United States), the Science and Technology Facilities Council (United Kingdom), the National Research Council of Canada (Canada), CONICYT (Chile), the Australian Research Council (Australia), the Ministerio da Ciencia e Tecnologia (Brazil), and the Ministerio de Ciencia, Tecnologia e Innovacion Productiva (Argentina).

1. INTRODUCTION

The angular momentum distribution of material within in a protogalactic halo affects the mechanics and timescale of structure formation in that halo (e.g. van den Bosch et al. 2002). The steady accretion of gas with progressively higher angular momentum with time causes disks to form from the inside–out, and the rate of growth will depend on the angular momentum distribution in the host halo. Simulations in which gas in an isolated, spherical dark matter-dominated halo undergoes a dissipative collapse produce a disk that grows throughout the age of the Universe at a rate of $\approx 0.7 \text{ kpc Gyr}^{-1}$ (e.g. Roskar et al. 2008).

A prolonged period of disk assembly is consistent with observations. The most direct evidence of outward disk growth comes from studies of the size evolution of disks over a range of redshifts (e.g. Trujillo & Agerri 2004; Trujillo & Pohlen 2005). Age and metallicity gradients are also a natural consequence of inside–out disk formation, with the oldest luminosity-weighted ages and most chemically enriched material expected at small radii. Bell & De Jong (2000) find evidence for such systematic gradients in nearby galaxies, while the outer regions of disks in a significant fraction of nearby spirals have an ultraviolet (UV) spectral-energy distribution (SED) that signals relatively young (at least in relation to smaller radii) luminosity-weighted ages (e.g. Zaritsky & Christlein 2007). Looking at galaxies within the Local Group, significant amounts of infalling gas are required to model the chemo-photometric properties of the outer regions of M33. The rate of gas accretion in that galaxy appears to have peaked 3 – 7 Gyr in the past, with more subdued accretion rates during the past 3 Gyr (Barker & Sarajedini 2008).

Changes in disk properties are not spurred exclusively by the accretion of new material. Secular processes re-distribute angular momentum between stars and gas, and objects that gain angular momentum migrate to larger radii (e.g. Sellwood & Binney 2002), pushing the disk boundary even further outwards (Aguerri, Balcells, & Peletier 2001). Galaxies also do not evolve in isolation, and interactions with companions will mix the stellar content of disks, changing the amplitude of (or even completely obliterating) radial trends in disk properties that were imprinted early-on, while also altering the thickness of the disk (e.g. Hayashi & Chiba 2006). Major interactions also extend the timescale of disk assembly, as the net angular momentum content of surviving halos grows with time (e.g. D’Onghia et al. 2006). Evidence that the evolution of a typical disk galaxy is affected by mergers – even during recent epochs – comes from the morphologies of galaxies at intermediate redshift (Hammer et al. 2005) and the angular momentum content of nearby disk galaxies (Hammer et al. 2007), which together suggest that the majority of nearby spiral galaxies experienced significant mergers in the last few Gyr. Still, that the star-forming histories of massive spiral

galaxies at intermediate epochs can be represented by models that assume passive evolution suggests that the impact of mergers is dampened on timescales that are substantially shorter than the Hubble time (Buat et al. 2008).

Studies of resolved stars in the outer regions of nearby spiral galaxies are of key importance for furthering our understanding of disk evolution, and the Centaurus Group (CG) contains prime targets for detailed investigation. Many galaxies in the CG show signs of on-going or recently elevated SFRs, signalling that this group may be in a state of active dynamical evolution. One such galaxy is M83, which is the largest spiral in the CG, and is the center of one of the two galaxy concentrations in the CG (Karachentsev et al. 2002). M83 is experiencing starburst activity (Bohlin et al. 1983), with a present-day SFR of $3 - 4 M_{\odot} \text{ year}^{-1}$ (Boissier et al. 2005).

The bulk of the HI in M83 is in a thin disk, although there is a kinematically distinct, thick HI disk containing 5.5% of the total HI within the central 8 kpc (Miller, Bergman, & Wakker 2009). Still, the bulk of the interstellar medium (ISM) in the inner disk of M83 is in molecular form, accounting for 80% of the total ISM mass in the central 5 arcmin (Crosthwaite et al. 2002). The projected densities of CO and HI drop markedly at a radius of 5.5 arcmin (Crosthwaite et al. 2002). The drop in molecular gas content at large radii may partially be a consequence of low ISM pressure, which hinders the formation of molecular material (Crosthwaite et al. 2002). The decline in gas density is accompanied by warping of the disk (Rogstad, Lockhart, & Wright 1974; Huchtmeier & Bohnenstengel 1981), and the disappearance of prominent spiral structure.

The drop in the interstellar content at 5.5 arcmin does not herald the termination of the gas disk; rather, the gas disk of M83 extends well past the classical optical radius (Rogstad et al. 1974), and Huchtmeier & Bohnenstengel (1981) conclude that 80% of the total HI mass lies outside of the Holmberg radius. The HI at large radius may not be in a thin disk, as kinematic measurements suggest that the vertical scale height of stars in the outer disk of M83 flares, in a manner than is consistent with heating by interactions with sub-structures in the halo (Herrmann, Ciardullo, & Sigurdsson 2009). Still, the ISM reservoir at large radius in M83 has been the site of recent star formation, as observations made with GALEX detect UV light from diffuse and compact components at large radii (Thilker et al. 2005). The compact UV sources are star clusters and HII regions that coincide with peaks in the HI distribution where the ISM is near the local critical density for triggering star formation (Dong et al. 2008). The clusters in the outer disk have typical masses $\log(M_{\odot}) = 4.7$, with a substantial dispersion (Dong et al. 2008). While the mass distribution of clusters in M83 is similar to that in the outer disks of other spiral galaxies, the UV light in M83 extends to larger radii than in these other systems (Zaritsky & Christlein 2007).

Star formation in the outer regions of M83 has not been an exclusively recent phenomenon. The spectra of many outer disk clusters lack H α emission, suggesting ages in excess of 10 Myr. Ages estimated from spectral-energy distributions (SEDs) indicate that the majority of clusters have ages ≤ 350 Myr, and Dong et al. (2008) conclude that cluster formation has been on-going for at least 1 Gyr after accounting for selection effects that hinder the detection of older systems. Finally, HII regions in the outer regions of M83 have metallicities that are at least one third solar, and this is consistent with the current levels of star formation having been sustained over Gyr or longer time scales if there has been *in situ* enrichment (Bresolin et al. 2009). This being said, feedback from SNe and other secular processes may also re-distribute chemically enriched material throughout the disk, boosting the metallicity of peripheral disk regions to higher levels than if they had evolved as a closed system (e.g. Scannapieco et al. 2008).

The local SFR in M83 has varied with radius during recent epochs. The luminosity functions (LFs) of x-ray sources in the central regions and disk of M83 differ (Soria & Wu 2002), such that the nucleus appears to have experienced a more continuous recent star-forming history than the main body of the disk, where the star-forming activity has recently dropped. This trend of decreasing age with increasing radius does not extend to very large radii, where the azimuthally-averaged UV color of M83 becomes bluer with increasing radius, and a rich population of compact young clusters is seen (Thilker et al. 2005). The clusters in the outer disk of M83 are smaller than those in the classical disk, and the brightest outer disk clusters are 2 - 3 mag fainter in the FUV than their inner disk kin (Bresolin et al. 2009). The line emission in outer disk HII regions is typically powered by a solitary O star, as opposed to the $\sim 10^2$ such stars that power HII regions at smaller radii (Bresolin et al. 2009).

The inner and outer regions of the M83 disk may also have experienced systematically different chemical evolution histories. While the analysis of spectra from HII regions indicate that there is an [O/H] gradient inside the Holmberg radius of M83, this trend does not continue to larger radii (Bresolin et al. 2009). Bresolin et al. (2009) argue that this chemical homogeneity may be a consequence of the low gas density at large radii. Drawing a parallel with low surface brightness (LSB) galaxies, which do not show large radial abundance gradients because star formation occurs sporadically, Bresolin et al. (2009) argue that a similar mechanism may be at work in the outer regions of M83. The material in the outer disk of M83 may also have been churned by tidal forces.

In the present study, stars that are evolving on the asymptotic giant branch (AGB) are used to probe the star-forming history of the outer disk of M83 during the past few Gyr. These stars are identified in deep near-infrared images obtained with NICI on Gemini South

(GS), and this is the first investigation in which individual stars are resolved in the outer regions of this galaxy. The adaptive optics (AO) capabilities of NICI, coupled with the ability to image at near-infrared wavelengths, make this instrument a powerful tool for probing the cool stellar contents of nearby galaxies. Because of their cool temperatures and the impact of line blanketing on the visible spectral-energy distributions (SEDs) of even moderately metal-rich evolved stars, AGB and RGB stars are arguably best studied at near-infrared wavelengths. Studies of resolved stars also benefit greatly from the high angular resolution delivered by NICI. Finally, background galaxies are the dominant source of contamination in deep photometric surveys of this nature, and the ~ 0.1 arcsec angular resolution of these images is helpful for identifying these objects.

The paper is structured as follows. The observations and photometric measurements are discussed in §2, while the color-magnitude diagrams (CMDs) and luminosity functions (LFs) constructed from these data are discussed in §3. The spatial distribution of AGB and RGB stars is investigated in §4. A discussion and summary of the results follows in §5.

2. OBSERVATIONS, DATA REDUCTION, AND PHOTOMETRIC MEASUREMENTS

2.1. The NICI Observations

Deep near-infrared images of five fields in the outer disk of M83 were obtained with NICI (Artigau et al. 2008) during March and April 2009 as part of queue program GS2009A-Q-74; these were the first queue-scheduled observations made with this instrument. NICI uses natural guide stars (NGSs) as beacons for AO correction. The NICI AO system assumes that the dominant turbulent layer is at the same elevation as the primary mirror. A beamsplitter divides the light into a ‘blue’ and a ‘red’ light path. While a suite of beamsplitters will ultimately be deployed, at the time of these observations only the ‘50–50 H –band’ beamsplitter, which parses light into wavelengths longward and shortward of $1.85\mu\text{m}$, was installed. The detector in each light path is a 1024×1024 InSb array, with an angular scale of 0.018 arcsec pixel $^{-1}$; hence, each detector images 18×18 arcsec 2 on the sky.

Each field is centered on a star with $V < 14$, which serves as the NGS. The locations of the NGSs, which are indicated on the Digital Sky Survey image in Figure 1, allow a range of galactocentric radii in the outer south east quadrant of the galaxy to be explored. The right hand panel of Figure 1 shows the map of 1.6 cm emission from Tilanus & Allen (1993), and three of the NGSs sample parts of the sky that are either in or near prominent HI concentrations. The field centered on GSC06726-0259 is near a region of pronounced

FUV emission. Additional information about the guide stars is listed in Table 1. R_{GC} is the distance from the center of M83 measured in the disk plane, assuming (1) a distance modulus of 28.6 (Karachentseva et al. 2007), and (2) a position angle and disk inclination determined from the K -band image of M83 in the 2MASS Large Galaxy Atlas (Jarrett et al. 2003).

Most of the images used in this study were recorded simultaneously through H and K_s filters. With the exception of one field (see below), a single observation consisted of five 30 sec co-adds. Observations were obtained at five points along a linear dither pattern with 1 arcsec offsets. This dither pattern was employed to facilitate the suppression of cosmic-rays and the construction of the calibration frames that are required to remove interference fringes and the thermal signatures of warm objects along the optical path. The observing sequence was repeated multiple times to boost the S/N ratio of the final dataset, and the total exposure time is ≈ 2 hours field $^{-1}$ filter $^{-1}$.

The field centered on GSC 06726–00126 was the first to be observed, and these observations differed from those of the other fields, as the knowledge gained from these data was used to refine the overall observing strategy. The initial plan was to record images simultaneously in J and K_s . However, the GSC 06726–00126 observations revealed that the throughput of the 50–50 H -band beamsplitter in J is markedly lower than anticipated, and so data were recorded in H instead of J for the remaining fields. A series of J and H observations were subsequently obtained of the GSC 06726–00126 field with NICI in single channel mode, in which a mirror feeds all of the light to only one channel. The H -band photometry of this field is not as deep as for the other fields.

The initial processing of the images followed standard procedures. The first steps were dark-subtraction and the division by a flat field frame. The flat field frame was obtained from observations of a light source in the facility cassegrain calibration unit. A series of exposures were recorded with this source ‘on’ and ‘off’. The latter data monitor thermal emission from warm objects along the light path, and a final flat field frame for each filter was constructed by subtracting the mean of the ‘off’ exposures from the mean of the ‘on’ exposures, and then normalizing the result.

Interference fringes and signatures of warm objects along the optical path were removed by subtracting calibration frames that were constructed by median combining the science observations of each field in each filter. A DC sky level was subtracted from each observation prior to image combination to account for fluctuations in the background light. The point spread function (PSF) wings from the NGSs extend over a few arcsec, and these produce conspicuous artifacts in the calibration frames if they are not removed. A 0.45×0.45 arcsec running median filter was applied to the flat-fielded images to suppress the PSF wings, and

the results were subtracted from the flat-fielded images. A 0.45 arcsec filter size was selected as it was found not to affect the central portions of the PSF, while at the same time rejecting much of the light outside of the first diffraction ring. These ‘wing-suppressed’ images were combined to construct the thermal signature/interference fringe calibration frame for each field+filter combination.

The processed images of each field were aligned and the results were combined by taking the median intensity at each pixel location. The final step in the processing sequence was to trim the median-combined images to the area that is common to all exposures of a given field, typically leaving a $\sim 14 \times 14$ arcsec² area for photometric analysis. An example of the final processed data is shown in Figure 2, where the H-band image of GSC 06726-00259 is displayed. There is a region with a $\approx 1 - 2$ arcsec radius surrounding the NGS where speckle noise prevents the detection of faint objects. Point sources, which have FWHM ≈ 0.08 arcsec, are clearly seen at distances in excess of 2 arcsec from the guide star, and these are stars in the outer regions of M83.

2.2. Photometric Measurements

Stellar brightnesses were measured with the PSF-fitting routine ALLSTAR (Stetson & Harris 1988). PSFs were constructed using the DAOPHOT (Stetson 1987) *PSF* task, using sources selected based on brightness, compactness, and the absence of obvious neighbors. Faint objects close to PSF stars were removed in an iterative manner. The PSF extraction radius was 0.3 arcsec; while the PSF wings extend to larger radii, sky noise confounds efforts to trace this part of the PSF in all but the brightest stars. The radius for PSF-fitting was restricted to the central diffraction spike, where the contrast between the target and background sky signals is highest.

The photometric measurements were culled to remove objects with (1) fitting uncertainties computed by ALLSTAR, ϵ , that exceed 0.3 magnitudes, which excises objects for which photometry is problematic, (2) higher than average *epsilon* values when compared with other objects of the same magnitude, and (3) that are non-circular, as gauged by the DAOPHOT *ROUND* parameter. The first step sets the faint limit of the data, while the second and third steps remove objects that have a non-stellar appearance and/or are in very crowded environments. Speckle noise prevents the detection of all but the brightest objects within ≈ 2 arcsec of the NGS, and so stars in that region were not photometered. Objects that coincide with diffraction spikes were also deleted from the target list.

The light path towards any source in the field (except the guide star) does not sample

the same atmospheric cross-section as the guide star, and this is referred to as ‘anisoplanicity’. Anisoplanicity can complicate the construction of the PSF from single NGS AO-corrected data, depending on factors such as the field of view, the order of correction, and the atmospheric turbulence profile. The impact of anisoplanicity increases with angular distance from the NGS, with the result that the PSF varies with distance from the NGS. The impact of anisoplanicity is modest on photometric measurements made over angular scales of many arcsec from images recorded at good ground-based observing sites (e.g. Davidge & Courteau 1999).

A modest amount of anisoplanicity is evident in some of the images, and this is demonstrated in Figure 3, where composite H -band light profiles of stars in two radial distance intervals from GSC06726–00259 are compared. The PSF of sources with $r_{NGS} > 3.6$ arcsec, where r_{NGS} is the distance from the NGS, is $\sim 8\%$ broader than that of sources with $r_{NGS} < 3.6$ arcsec; the radial differences in FWHM are smaller in the K -band data. The uncertainty in the FWHM measurements, estimated from bootstrap re-sampling, is ± 0.003 arcsec, indicating that the FWHMs of the PSFs differ at roughly the 2σ level.

Two sets of photometric measurements were made for each field: one set used a fixed PSF for each filter, and the other a spatially variable PSF. In the latter case it was assumed that PSF variations across the field follow a quadratic polynomial. The fixed and variable PSFs were constructed from the same stars to prevent introducing possible systematic effects when comparing the results. The photometry obtained with the variable PSF fit was adopted only if it produced a CMD with a smaller dispersion than the results obtained with the fixed PSF.

The CMDs of the GSC06726–0259 field generated from fixed and variable PSFs, which are compared in Figure 4, showed the greatest differences. The application of a variable PSF reduces the dispersion in the CMD, and similar results were found for the GSC06726–0266 field, but not for the remaining fields. Therefore, a variable PSF was used to construct the final CMDs of the GSC06726–249 and 266 fields, while a fixed PSF was used for the other fields.

The photometric calibration was defined using the brightnesses and colors of the NGSs listed in the 2MASS Point Source Catalogue (Cutri et al. 2003). The NGSs are saturated in the long-exposure science observations, and so the calibration measurements were made from short exposure observations that were interleaved with the longer-exposure observations throughout the observing sequence. This strategy was adopted so that the short exposure calibration images sample roughly the same range of Strehl ratios as the science data. The short exposure images were recorded with the AO system running.

If the Strehl ratio exceeds $\sim 0.05 - 0.1$, then the center of the PSF is dominated by a prominent spike, the width of which roughly matches the telescope diffraction-limit (the agreement with the theoretical diffraction limit is not exact, as optical aberrations and residuals in image motion that are not corrected due to the limited bandwidth of the AO system broaden this feature). This central spike sits on a much more extended component, that is modulated at intermediate radii by the Airy pattern, and is spread over an angular scale that is comparable to that of the ‘seeing’ disk. Calibration measurements that rely only on information in the central diffraction spike are uncertain due to Strehl ratio variations, such that $\epsilon_{cal} \approx \Delta S$, where ϵ_{cal} is the uncertainty in the calibration in magnitudes, and S is the Strehl ratio. While more robust calibration measurements can be obtained using very large apertures, the results may then be affected by crowding, or uncertainties in the flat-field. There are also pragmatic difficulties in translating measurements made with a large aperture to measurements made with a much smaller PSF-fitting radius.

For the current data, the calibration is based on photometry within the PSF radius (0.3 arcsec – see above). The fraction of light outside of the 0.3 arcsec radius will change with seeing, and this will introduce scatter in the frame-to-frame measurements, as well as in the width of the sequences on the CMDs. This calibration procedure has been found to produce excellent agreement with measurements made from non-AO corrected data (e.g. Figure 4 of Davidge 2007). After accounting for beamsplitter throughput, the photometric zeropoints computed for NICI in this manner agree with those measured for Hokupa’a + QUIRC at Gemini North to within a few tenths of a magnitude.

The final science images were constructed from data that were typically recorded over at least 2 hours, and so Strehl ratio variations that occur over times scales of many minutes or less tend to average out. In fact, the scatter in the H and K zeropoints during any given night was typically $< \pm 0.1$ mag, and this sets an upper limit to the reliability of the calibration. Evidence that the calibration is reliable to within a few percent comes from the mean $H - K$ colors computed from the various fields, which agree to within 0.006 ± 0.021 magnitude (§3.1.2).

3. RESULTS

3.1. The $(K, H - K)$ CMDs

3.1.1. The General Appearance of the CMDs and the Impact of Anisoplanicity

The $(K, H - K)$ CMDs of the five fields are shown in Figure 5. There are field-to-field differences in source density, as might be expected given the range in R_{GC} (Table 1). The lowest stellar density is in the GSC06726–0067 field, which has the highest R_{GC} , while the GSC06726–0259 field, which is close to an area of prominent UV emission, may be deficient in objects at the bright end.

The number of objects in each field is modest, making it difficult to identify coherent trends. However, this changes when data from multiple fields are combined. A composite CMD of all fields is shown in the lower right hand panel of Figure 5, and objects with $K < 22$ define a locus that is populated predominantly by AGB stars (§3.1.2). The composite CMD also broadens and becomes more richly populated when $K > 22$, possibly due to the onset of the RGB.

GSC06726–00126 and GSC06726–0181 have the smallest R_{GC} and are located on the sky close to the south east spiral arm of M83. These fields are thus most likely to have the highest levels of contamination from stars in the classical disk of M83, and their stellar contents might then be expected to differ from those of the other fields that have larger R_{GC} . In fact, the bright sequences in the CMDs of these two fields appear to be tilted from vertical, whereas the bright sequences in the other three fields are close to vertical. This being said, the normal points of the fields with the smallest and largest R_{GC} are not significantly different (§3.1.2).

Anisoplanicity introduces scatter in the photometry; even though the photometry was obtained with a variable PSF in some fields, residual variations in the ability to track the PSF are undoubtedly present, and these are a source of scatter in the CMDs. One way to check for systematic effects due to PSF variations is to examine the CMDs of stars at different offsets from the guide star. The CMDs of objects in two radial intervals near GSC06726–0259 are shown in the right hand panel of Figure 4. There is excellent agreement between the CMDs defined by the stars in the two radial intervals. An examination of the CMDs of sources at various radial intervals in the other fields also did not find evidence for radial variations in either the mean color or breadth of the stellar sequence. These comparisons suggest that any systematic errors due to anisoplanicity are ≤ 0.1 magnitude in all of the fields.

Random noise, coupled with spatial variations in the PSF that are not tracked by

DAOPHOT, introduce scatter in the photometric measurements. Artificial star tests, in which scaled versions of the PSFs are added to the data, were run to estimate the dispersion arising from random noise. The artificial stars were assigned the color of the dominant stellar locus in each field. As with the photometry of real stars, artificial stars were only considered to be recovered if they were detected in both passbands.

An upper limit to the scatter that PSF variations contribute to the CMDs can be obtained by comparing the observed scatter with that predicted from the artificial star experiments. Only an upper limit to the scatter is obtained, as star-to-star variations in age and/or metallicity, coupled with stellar variability, broaden the stellar locus on CMDs. At $K = 21$, the scatter in $H - K$ predicted from the artificial star experiments agrees with that seen among M giants in fields GSC06726–0181 and 0259, indicating that PSF variations in these fields are not significant when compared with random noise at this magnitude. As for the GSC06726–0126 and 0266 fields, there is a residual dispersion of ± 0.1 magnitude in $H - K$ at $K = 21$, indicating that PSF variations introduce scatter of no more than this amount. The situation changes at fainter magnitudes. At $K = 22$ the measured dispersion in $H - K$ exceeds that predicted from the artificial star experiments in all four fields. Given that the scatter introduced by PSF variations will not change with magnitude, then the increased scatter at $K = 22$ indicates that there is a substantial mix in the age and/or metallicity of stars at this magnitude in all fields.

3.1.2. Comparisons with isochrones and the K/M giant AGB content

The ($M_K, H - K$) CMDs of two field groupings, one consisting of GSC06726–0126 and 0181 (‘inner disk’), which are close together on the sky and have the smallest R_{GC} , and the other of the remaining fields (‘outer disk’), are compared in Figure 6. A distance modulus of 28.6, as computed by Karachentsev et al. (2007) from the brightness of the RGB-tip, has been assumed. As for extinction, the Schlegel, Finkbeiner, & Davis (1998) maps give $A_B = 0.28$ for M83. This is a lower limit to the total extinction, as it does not include dust that is internal to M83. In fact, the outer regions of at least some spiral galaxies appear to contain significant amounts of dust. Popescu et al. (2005) find that the ratio of FIR to UV flux in M101 decreases with increasing radius, and interpret this as a radial gradient in attenuation. In the case of M83, the $8\mu\text{m}$ emission from the star-forming knots in the outer disk of M83 is predominantly stellar in origin, suggesting that there is little interstellar dust in these clusters (Dong et al. 2008). Still, there is evidence for significant dust extinction outside of these clusters. Boissier et al. (2005) compute radial extinction profiles for M83 using three different indicators: (1) the ratio of Balmer line strengths, (2)

the ratio of the total IR flux to the FUV flux, and (3) the slope of FUV SED. All three estimators predict that the attenuation reaches a minimum of $A_{FUV} = 1.5$ magnitudes at a radius of 200 arcsec, before climbing with increasing radius out to at least 6 arcmin. These three extinction indicators agree out to a radius of 250 arcsec, but at larger radii the Balmer line ratio predicts a much larger increase in extinction towards larger radii than the other two; in contrast, the extinction estimated from the slope of the UV SED may decrease at very large radii, although there are substantial error bars in these measurements. As a compromise between these two extremes, the extinction computed from the total-IR/FUV ratio with $A_{FUV} = 1.6$ magnitudes (the mean at large radii in Figure 2b of Boissier et al. 2005) is adopted here, and has been applied to the data points in Figure 6. This corresponds to $A_V = 1.4$ magnitudes and $A_K = 0.16$ magnitudes.

To facilitate the comparison of any general trends, mean $H - K$ colors were computed in ± 0.25 magnitude bins in K in the inner and outer disk CMDs, and the results are shown in Figure 6. A 2.5σ rejection scheme was applied to suppress outliers, and stars with $(H - K)_0 > 0.45$, which are either C stars or background galaxies, were not included when computing the mean colors. The error bars show the standard error in the mean color. The mean difference between the normals computed for the inner and outer disk fields is $\Delta(H - K) = 0.006 \pm 0.021$ magnitudes, in the sense of outer – inner disk color. Therefore, the mean colors of the inner and outer disk sequences are not significantly different.

Isochrones with $Z = 0.004$ and $Z = 0.019$ from Girardi et al. (2002) are plotted in Figure 6. These isochrones span the range of metallicities inferred from $[O/H]$ measurements of HII regions in the outer disk (e.g. Bresolin et al. 2009). Figure 4 of Bresolin et al. (2009) summarizes $[O/H]$ measurements in the outskirts of M83, and there is considerable scatter due to calibration uncertainties. The majority of calibrations indicate that $[O/H]$ in the outer disk of M83 is within $\sim 0.1 - 0.2$ dex of solar ($Z = 0.010 - 0.013$ if oxygen is assumed to trace all metals). There is an $[O/H]$ gradient in the disk of M83, and these same calibrations predict a super-solar metallicity for the inner disk of M83. There is one calibration that yields $[O/H]$ values that are markedly lower than the others, and this predicts that the outer disk has $[O/H]$ that is 0.4 dex lower than solar ($Z = 0.006$ if oxygen traces all metals).

While detailed abundance studies of the chemical compositions of bright stars will ultimately provide the information needed to confirm the metallicity scale in M83, there is a hint that the youngest stars in the classical disk of M83 may have a metallicity that is higher than solar. The ratio of Wolf-Rayet stars with carbon dominant (WC) to nitrogen dominant (WN) atmospheres is higher in M83 than in the Galaxy, and this may be due to a higher metallicity in M83, and the consequent impact on stellar mass loss rates (Crowther et al. 2004; Hadfield et al. 2005).

Photometric variability in highly evolved AGB stars introduces uncertainties when comparing observations with models, and there are also uncertainties in the model physics. This being said, the isochrones indicate that many of the stars with $M_K < -6.8$ are evolving on the AGB, and that those with $M_K < -7.8$ have ages ≤ 10 Gyr. The mean color of stars at $M_K = -8$ thus provides some insight into metallicity, since these stars should not have colors that place them above very old isochrones. The mean colors of stars in the three outer disk fields at $M_K = -8$ coincides with the 10 Gyr $Z = 0.004$ models, suggesting that $Z > 0.004$ in the outer disk. Small number statistics are an issue for the two inner disk fields, as there are fewer stars in these fields with $M_K \approx -8.0$. Based on the presence of stars with $M_K \approx -8$, the three outer disk NICI fields contain stars that formed within the past few Gyr, in broad agreement with the age distribution of star clusters (e.g. Dong et al. 2008), as well as the K -band LF of the outer disk fields, which is compared with models in §3.3. It thus appears that intermediate age stars in the outer regions of M83 are not confined to star clusters; rather, these stars are distributed throughout the outer disk.

3.1.3. *C stars*

The isochrones shown in Figure 6 assume oxygen-rich atmospheres, and so do not track the evolution of stars with carbon-rich atmospheres. Cool, bright C stars form in systems with ages \leq a few Gyr (e.g. Maraston 2005), and occupy an area of the near-infrared CMDs that extends redward of M giants (i.e. evolved stars with oxygen-rich atmospheres). With the caveat that comparatively warm C stars may mingle with M giants in near-infrared CMDs, cool C stars can be identified based on their near-infrared photometric properties.

For this study, C star candidates are identified using the photometric properties of C stars in the LMC as a guide. The area of the LMC ($K, H - K$) CMD that contains C stars is marked in Figure 6. The upper and lower boundaries of the C star area, as well as the blue limit of the C star sequence, were determined from the envelope of the C star locus in the ($K, J - K$) CMD discussed by Nikolaev & Weinberg (2000) in their study of the LMC. These boundaries were transformed onto the ($K, H - K$) plane using a (J-K) to (H-K) color transformation based on observations of Galactic and LMC/SMC C stars.

There are a number of sources in the NICI fields with photometric properties that are consistent with them being C stars. However, some of these are probably background galaxies, the majority of which form a diffuse sequence with $H - K \approx 0.8$ at these magnitudes (e.g. Davidge 2008). Upper limits on contamination from background galaxies can be deduced from the GSC06726–0067 field, where there are three objects in the C star regions of the ($K, H - K$) CMD. If all three are background galaxies, then 12 ± 7 background objects

would be expected in the other NICI fields. For comparison, 26 objects fall within the LMC C star regions in these four CMDs, and so there is an excess of 14 ± 9 objects over that expected from presumed background objects. This is a lower limit to the actual number of C stars, as some of the red objects near GSC06726–0067 may be C stars that belong to M83. This comparison suggests that C stars are present in the fields observed with NICI, and such objects are evidence of field stars with an age of a few Gyr in the outer regions of M83.

The relative numbers of C stars and M giants in a system depends on the metallicity and age distributions, and so the ratio of C stars to M giants, C/M, is a probe of stellar content. The metallicity $Z = 0.008$ is a benchmark for efforts to model C/M as the evolutionary flux measurements for TP-AGB evolution can be calibrated from LMC cluster star counts. If stars that formed in the outer disk of M83 for the past $\sim 1 - 2$ Gyr did so from material that had a metallicity that is no higher than $Z = 0.008$, then the fuel consumption rates compiled by Maraston (2005) predict that all of the fuel consumed during TP evolution is done so while the star has an atmosphere with $C/O > 1$; that is, all TP-AGB stars that formed between 1 and 2 Gyr should be C stars. Using calibrating relations from Maraston (2005), Davidge (2010) concludes that $C/M = 2.4$, where M is the number of thermally-pulsing (TP) AGB M giants, for a $Z=0.008$ system that has had a constant SFR.

The C/M ratio in M83 was measured following the procedures described by Davidge (2010), but adjusted for the use of $H - K$ colors. The regions of the CMD in which TP-AGB M giants and C stars were counted are indicated in the right hand column of Figure 6. TP-AGB M giants are assumed to have $(H - K)_0$ between 0 and 0.45 and M_K between -9.5 and -7 ± 0.5 . The former is the approximate peak magnitude of the AGB, whereas the latter is the approximate point at which evolution on the TP-AGB commences for intermediate age stars. Based on the photometric properties of C stars in the LMC, C stars are assumed to have $(H - K)_0 \geq 0.40 \pm 0.05$ and M_K between -7 and -9 .

The C/M ratios calculated with the criteria described in the preceding paragraph are listed in Table 2. The uncertainties combine counting statistics with the range in star counts that result from the ± 0.5 magnitude dispersion in the faint magnitude limit for TP M giants, and the ± 0.05 magnitude dispersion in the blue boundary used to identify C stars. The rows labelled ‘Composite’ show the C/M ratios for the inner and outer disk groupings.

Small number statistics render the errors in C/M large. Still, with the possible exception of the GSC06726–0067 field, the C/M ratio does not vary significantly from field-to-field. This is consistent with the majority of the fields having experienced similar star-forming histories during intermediate epochs. While this may seem contradictory to the conclusions that will be drawn in §4, where it is argued that there is a substantial difference in stellar content between the inner and outer disk fields, the differences in stellar content that are

discussed in §4 occurred during epochs that are not those during which substantial numbers of bright C stars are produced.

The C/M ratios for the composite data sets are lower than predicted for a $Z=0.008$ system that has had a constant SFR. Two possible explanations for this difference, involving a metallicity that is higher than $Z = 0.008$ or a star-forming history that is not constant, are considered below. In reality there will almost certainly be an interplay between both of these, and the following discussion is meant to demonstrate the extent to which metallicity and star-forming history influence C/M.

The number of C stars will be lower than predicted if the outer regions of M83 have $Z > 0.008$, as suggested by the analysis of emission lines in HII regions (Bresolin et al. 2009). Maraston (2005) argues that the number of C stars scales inversely with metallicity, such that the number of C stars in a system with $Z = 0.016$ will be one half that in a $Z = 0.008$ system, while the number of M giants will increase. If this is the case then $C/M \approx 0.7$ for solar metallicities, which is much closer to what is measured in the outer disk of M83.

If the actual SFR has not been constant then this will also influence C/M. A lower SFR 1 – 2 Gyr in the past compared with that during the most recent 1 Gyr would result in a lower C/M ratio, as the stars that formed within the past 1 Gyr are too massive to have dredged up sufficient C into their atmospheres to make them C-rich for a large fraction of their TP-AGB lifetimes. While there are as yet no independent probes of the SFR in the outer regions of M83 1 – 2 Gyr in the past, such as very deep CMDs, Boissier et al. (2005) find that the global SFRs derived from the slope of the UV-SED and from the $H\alpha$ flux are in good agreement, suggesting that the present-day SFR is comparable to that averaged over the past Gyr – unless M83 is being viewed at a special epoch then the SFR probably has been constant over the past Gyr. If the epoch of constant SFR continued up to 2 Gyr in the past then the C/M ratio in M83 is consistent with a solar (or higher) metallicity.

3.1.4. *Red supergiants*

The outer disk of M83 contains a large number of star clusters with ages < 100 Myr (Dong et al. 2008); for comparison, the age distribution of clusters in the main body of the inner disk peaks near 30 Myr (Jensen, Talbot, & Dufour 1981). The fraction of red supergiants (RSGs) with respect to AGB stars might be expected to grow with R_{GC} in the outer disk of M83, given the gradient in UV color found by Thilker et al. (2005). Indeed, the UV color measurements made by Thilker et al. (2005) suggest that the mean luminosity-weighted age near GSC06726–0067 ($R_{GC} = 14.5$ kpc) is only a few tens of Myr. It might

then be anticipated that some of the bright stars in the NICI CMDs are RSGs. Of course, the field between clusters may not provide a representative census of the youngest RSGs, as the most massive stars may not live long enough to diffuse from their place of birth, hindering the detection of bright RSGs outside of their natal clusters. This is exacerbated by the low density of the outer disk environment, which should result in longer diffusion time scales at larger radii when compared with smaller radii (e.g. Johnston, Hernquist, & Bolte 1996). Yet another complication is that the locations of bright AGB stars and RSGs overlap on near-infrared CMDs, and only those RSGs with relatively blue colors stand out. If they are in dusty star-forming regions, then even young, intrinsically blue RSGs may be reddened to the point that they masquerade as AGB stars.

Solar metallicity isochrones from Girardi et al. (2002) with ages of 10, 30, and 100 Myr are compared with the inner and outer disk composite CMDs in Figure 7. Both CMD groupings contain objects with $(H - K)_0 < 0.2$ and $M_K < -7$ that are candidate RSGs, suggesting that both fields contain stars that formed within the past 100 Myr. If, as suggested by the UV colors (Thilker et al. 2005), there is an age gradient in the outer disk such that younger luminosity-weighted ages occur at larger R_{GC} , then a higher fraction of bright RSGs might be expected in the GSC06726–0067, 249, and 266 composite CMD (but see the caveat in the preceding paragraph regarding diffusion). In fact, the outer disk regions *do* contain objects with RSG-like colors that are brighter than those in the inner disk field, although the statistical significance is modest. Considering the region of the CMDs with $M_K < -7.5$ and $H - K$ between 0 and 0.2, there are 5 objects in the outer disk CMD, but none in the inner disk CMD. The presence of RSGs notwithstanding, the majority of stars near GSC06726–0067, 0259, and 266 have $H - K$ colors that are too red for them to be RSGs, indicating that there is an underlying substrate of stars with ages ≥ 0.2 Gyr in these fields.

3.1.5. *Red giant branch stars*

The RGB forms a prominent sequence in the CMDs of systems with ages in excess of a few Gyr. The 10 Gyr isochrones predict that the RGB-tip occurs near $M_K = -6.4$ if $Z = 0.004$ and $M_K = -6.9$ if $Z = 0.019$; thus, moderately metal-rich RGB stars are well within the detection limits of the NICI data. In fact, there is an increase in the number of objects with $M_K < -6$ and $H - K \sim 0.3$ in the composite GSC06726–0126 and 0181 CMD in Figure 6. Still, the magnitude at which these sources appear is not consistent with that expected for the moderately metal-rich RGB that is expected in disks (§3.3). These faint red objects are not background galaxies, as the GSC06726–0067 field, which has the largest R_{GC} and the lowest source density, contains only a modest number of sources fainter than $M_K = -6$.

3.2. *JHK* Observations of GSC 06726–0126 Field

The *J* observations provide additional information for investigating the near-infrared spectral-energy distribution (SED) of sources in the GSC 06726–0126 field. The $(K, J - K)$ CMD of the GSC 06726–0126 field is shown in the left hand panel of Figure 8. Comparisons are made with $Z = 0.019$ isochrones from Girardi et al. (2002) in the right hand panel of Figure 8. As with the $(K, H - K)$ CMDs, the observed stellar sequence cuts diagonally across the isochrones, falling redward of the 1 Gyr isochrone at the bright end, and blueward of this sequence at the faint end.

The portion of the LMC $(K, J - K)$ CMD from Nikolaev & Weinberg (2000) that contains C stars is indicated in the right hand panel of Figure 8. There are a number of sources in this part of the CMD, as expected from the $(K, H - K)$ CMD of the same field, and it is likely that the majority of these are C stars. Indeed, if the majority of these objects were background galaxies then the numbers of objects with $J - K \geq 1.5$ would increase steadily towards fainter magnitudes, with no break in counts near $M_K \approx -7$. In contrast, the number of objects in Figure 8 with $J - K > 1.5$ dominates when $M_K > -7$.

The $(H - K, J - H)$ two color diagram (TCD) provides a means of comparing the near-infrared SEDs of sources. The location of stars on the near-infrared TCD is sensitive to surface gravity and metallicity, in large part because deep ^{12}CO and H_2O absorption features dominate the near-infrared light from stars with surface gravities that are near the lower and upper limits that occur in stars. The near-infrared TCD of sources near GSC 06726–0126 is shown in Figure 9. Only objects with $K < 22$ are plotted to limit scatter due to photometric errors. Fiducial sequences of stars evolving on the main sequence and on the AGB from the 1 Gyr $Z = 0.019$ Girardi et al. (2002) isochrones are also indicated. The majority of sources in the TCD have $J - H > 0.7$, which is larger than expected for main sequence stars, but is consistent with that expected for cool evolved stars with low surface gravity. The model AGB sequence passes through the data cloud for sources with $J - K < 1.5$. The locus of LPVs in the SMC and LMC, based on data given by Wood et al. (1983; 1985), is also shown, and some of the stars in M83 have near-infrared SEDs that are consistent with them being LPVs. The comparisons in Figure 9 thus indicate that foreground stars are not present in large numbers, and that the sources found here have SEDs that are consistent with those of evolved stars.

3.3. The K Luminosity Functions

The K luminosity functions (LFs) of objects with $(H - K)_0$ between -0.05 and 0.45 are shown in Figure 10. $n_{0.5}$ is the number of sources arcsec^{-2} per 0.5 magnitude interval. The turn-down at the faint end of the LFs is due to incompleteness. At the bright end there is a general tendency for the number counts to decline towards brighter magnitudes, although the LFs of the GSC06726–0126 and 0181 fields are relatively flat in the interval between $M_K = -6$ and $M_K = -8$.

The mean LFs of the GSC06726–0126 + 0181 and GSC06726–0259 + 0266 fields are shown in Figure 11. The CMDs of these fields are also shown to allow features in the LFs to be related to those in the CMDs. There is modest contamination from background galaxies, and the LFs were corrected for this in a statistical manner. A power-law was fit to the GSC 06726–0067 LF in the interval between $M_K = -6$ and -9 , and the result – which is shown in the top panel of Figure 10 – was subtracted from the composite LFs. Some of the sources near GSC06726–0067 are almost certainly stars belonging to M83, and so this procedure overestimates background galaxy contamination. In any event, the background galaxy correction has only a minor impact on the LFs shown in Figure 11.

The LFs of the two field groupings in Figure 11 differ. Whereas the GSC06726–0259+0266 LF follows a single power-law from $M_K = -7.5$ to $M_K = -5.5$, there is a break in the number counts at $M_K = -6$ in the GSC06726–0126 + 0181 LF. This change in number counts corresponds to a broadening of the CMDs of the GSC06726–0126 and 0181 fields that exceeds that expected from photometric errors, and signals the presence of stars with a range of ages and/or metallicities (§3.1.1). The flat nature of the inner disk LFs at the bright end has already been noted, and the number counts in the inner disk LFs appear to dip slightly in the interval immediately above the break; this behaviour is seen in the individual LFs of the GSC06726–0126 and 0181 fields (Figure 10).

Model LFs for solar metallicity simple stellar populations were constructed to gain insight into the stellar content in these fields, and the models are compared with the observed LFs in Figure 12. These models were constructed from the Girardi et al. (2002) isochrones using routines in the STARFISH (Harris & Zaritsky 2001) package. The models indicate that the localized dip in number counts above the RGB that occurs in the inner disk LFs is a characteristic of systems with ages 1 – 2 Gyr. Indeed, a similar local minimum in star counts occurs above the RGB-tip in M32 (Davidge 2000), which is a galaxy that contains a large intermediate age population (Davidge & Jensen 2007, and references therein).

The inner disk LF appears to have characteristics that are indicative of a mix of the $\log(t_{yr}) = 9.0$ and older LFs. In contrast, the LF of the outer disk is well-matched by the

$\log(t_{yr}) = 8.5$ LF. The model LFs thus suggest that the brightest stars in the inner disk fields tend to be older than those in the outer disk fields.

If these data contain a substantial old population then the RGB-tip might produce a noticeable feature in the LF. To better assess if such a feature is present, LFs were calculated with 0.2 magnitude binning, and the results are shown in the top two panels of Figure 13. The LFs of the inner and outer disk field are significantly different. The GSC06726–0259+0266 LF follows a single power-law over the magnitude range shown in this figure, and a least squares power-law fit is compared with the LF in Figure 13. This power-law was scaled to match the number of points in the GSC06726–0126+0181 fields, and then subtracted from the composite LF of these fields. The resulting differences between the least squares fit and the composite inner disk LF, Δ , are shown in the third panel of Figure 13. The Δ values in three bins differ from zero at more than the 2σ level, and it is clear that the power-law that characterizes the GSC06726–0259+0266 LF is not an adequate representation of the GSC06726–0126+0181 LF.

The composite LFs were convolved with a three-point Sobel edge-detection filter, and the Sobel-convolved GSC06726–0126+0181 LF is shown in the bottom panel of Figure 13. The Sobel-convolved LF of GSC06726–0259+0266 shows much smaller bin-to-bin deviations than in GSC06726–0126+0181, and the dotted lines in Figure 13 indicate the $\pm 1\sigma$ variance about the mean convolved signal from that LF. The scatter in the Sobel-convolved GSC06726–0259+0266 LF provides an upper limit to the noise in the edge detection signal. Using this estimate, the break near $M_K = -5.8$ in the GSC06726–0126+0181 LF is significant at the 3.6σ level.

Is the change detected in the LF by the Sobel filter due to the RGB-tip? The good agreement between the inner disk LF and the $\log(t) = 9$ model in Figure 12 strongly suggests that the edge-detection filter is picking up structure in the LF that is due to AGB evolution and/or the recent star-forming history. Still, the change in character of the inner disk CMDs at the faint end is consistent with the onset of RGB stars (§3.1.5). The break in the GSC06726–0126+0181 LF also has an amplitude of 0.3 – 0.4 dex, and thus is comparable in strength to the RGB-tip discontinuity in the disk of NGC 6822 (Davidge 2003), a galaxy that – like M83 – has formed stars throughout its lifetime (e.g. Tolstoy et al. 2001).

Perhaps most significantly, the M_K of the break is not consistent with that expected from an old moderately metal-rich disk population. Ferraro et al. (2000) define an empirical calibration from Galactic globular clusters that relates metallicity and RGB-tip brightness in old populations. RGB-tip brightnesses computed from this calibration are indicated at the top of Figures 11 and 13. While this calibration is strictly applicable only to old systems, the RGB-tip brightness changes only slightly with time for ages in excess of a few Gyr, and

so it also holds approximately for intermediate age populations.

If the break in the GSC06726–0126 and 0181 field LFs is due to the RGB-tip then the Ferraro et al. (2000) calibration suggests that $[M/H] \sim -1.8 \pm 0.1$. The quoted uncertainty reflects the LF binning. This metallicity estimate is that of the dominant, presumably ‘old’, population, and is much lower than what would be expected from a disk population. It should be noted that if the majority of RGB stars formed within the past few Gyr then the Ferraro et al. (2000) calibration predicts an RGB-tip luminosity that is too bright, in which case $[M/H]$ inferred from the Ferraro et al. (2000) calibration is a lower limit to that of the dominant population. Small number statistics may also bias the RGB-tip magnitude to fainter values than would be seen in more populous systems (e.g. Crocker & Rood 1984).

4. THE SPATIAL DISTRIBUTION OF AGB STARS: EVIDENCE FOR AN AGE GRADIENT IN THE OUTER DISK

4.1. Radial Trends in the Star Counts

Disk light profiles can be sorted into three broad types, based on their behaviour at large radii (e.g. Pohlen & Trujillo 2006). Type I disks have light profiles that follow a single exponential. While the classical exponential profile was once thought to be the norm for disks, with any break in the light profile at large radius associated with the physical truncation of the stellar disk (e.g. van der Kruit & Searle 1981), recent surveys have found that only $\sim 10\%$ of spiral galaxies have Type I profiles. Type II and III disks have profiles that break either down (‘truncated’) or up (‘anti-truncated’) at large radii, respectively.

An important caveat when interpreting this classification scheme is that light is only a crude proxy for mass. Bakos, Trujillo, & Pohlen (2008) suggest that the break in Type II light profiles may be due to a change in stellar content induced by the physics of star formation in low density environments, rather than a structural change in disk properties. They conclude that, despite having different light profiles, the mass profiles of Type I and II disks may be similar. The similar kinematic properties of PNe in the outer regions of M83 and M94, which are galaxies that have very different light profile characteristics at large radii (Herrmann et al. 2009), is consistent with this.

Resolved stars provide a more direct probe of stellar content than integrated light. The spatial distribution of stars with $K \leq 22.5$ in the NIC1 fields is investigated in Figure 14, where projected stellar density is shown as a function of R_{GC} . The error bars show counting statistics. With the exception of the area around GSC06726–0067, the density of AGB stars is more-or-less constant between de-projected radii of 350 and 500 arcsec, with ≈ 0.2 stars

with $K < 22.5$ arcsec $^{-2}$. This is counter to the behaviour of the near-infrared light profiles of M83 measured by Jarrett et al. (2003), which break downward at $R_{GC} = 360$ arcsec. Thus, the distribution of bright red stars in the outer disk of M83 does not track the integrated near-infrared light.

The specific frequency (SF) measures the number of objects per unit integrated light. In the context of a simple stellar systems with ages ≥ 0.2 Gyr, the SF of AGB stars decreases with increasing age (e.g. Maraston 2005). Thus, higher AGB SFs correspond to younger luminosity-weighted ages.

In the current study, the SF is defined as the number of stars with $K < 22.5$ per $M_K = -16$ brightness, with the latter calculated from the Garrett et al. (2003) 2MASS K -band light profile. The SF measurements for the GSC06726–0126, 0181, 0259, and 0266 fields are shown in Table 3; GSC06726–0067 is too far from the center of M83 to have reliable 2MASS surface photometry, and so a SF was not computed for this field. The light profile was extrapolated by ~ 30 arcsec to compute the SF of the GSC06726–00259 field. There are field-to-field differences in the SFs of AGB stars; whereas the SF of AGB stars near GSC06726–0181 and 0266 are very similar, the SF of AGB stars around GSC06726–0126 is comparatively low, while the SF of AGB stars near GSC06726–00259 is very high.

If the stellar content throughout the main body of M83 is similar to that in the outer disk then the light profile of M83 can be transformed into an AGB number density profile by applying a scaling factor determined from calibration fields. For this study, the GSC06726–0126, 0181, and 266 fields, which are at radii where the K -band surface brightnesses are most secure, were used to set the calibration. The resulting AGB density profile predicted from this calibration is shown as the solid line in Figure 14.

A linear extrapolation of the solid line in Figure 14 to larger R_{GC} falls well below the AGB star densities measured near GSC06726–0259 and 0067. To the extent that light profiles can be extrapolated to larger radii then this suggests that the fraction of the total K -band light that originates from bright AGB stars changes with radius in the outer disk of M83, in the sense of increasing towards larger radii; the luminosity-weighted age thus drops (i.e. becomes younger) towards larger radii. This is consistent with the trend of bluer UV colors towards larger radii measured in M83 by Thilker et al. (2005), and the absence of an RGB-tip feature in the LF of stars near GSC06726–0259 and 0266. A similar trend of decreasing luminosity-weighted age with increasing radius is seen in the outer disk of M81 (Davidge 2009).

4.2. Star Counts as Probes of Stellar Content

The fraction of the K -band light that comes from AGB stars is a probe of stellar content. Based on the SFs listed in Table 3, AGB stars in the inner disk fields contribute on average only $\sim 20\%$ of the K -band light that comes from AGB stars in the outer disk fields. This can be used to estimate the difference in age between the inner and outer disk fields using the relation between the fraction of total K -band light from AGB stars and age computed by Maraston (2005) for simple stellar populations. The solar metallicity relation in Figure 13 of Maraston (2005) indicates that a difference in the contribution made by AGB stars like that between the inner and outer disk fields corresponds to an age difference of ~ 0.6 dex, or a factor of 4. If the luminosity-weighted age of the inner disk fields is a few Gyr, then the Maraston (2005) calibrations predict that RGB stars should contribute $\sim 6\times$ less light in the outer disk fields than in the inner disk fields. Thus, one would expect a much weaker RGB-tip feature in the outer disk LF than in the inner disk LF.

The SF measurements can be used to compare the stellar content of the outer disk of M83 with that of other disk systems in a purely empirical manner. Although it has a moderately low SFR at the present day, M31 is an interesting comparison object since there was more vigorous star-forming activity ≈ 1 Gyr in the past (e.g. Williams 2002). The structural properties of M31 also suggest that it is a ‘typical’ spiral galaxy in terms of the cumulative impact of interactions on its angular momentum content (Hammer et al. 2007).

The SF of stars in the M31 Disk 2 field, where the density of AGB stars with $M_K \leq -6$ is 0.50 arcsec^{-2} and the K -band surface brightness is $17 \text{ mag arcsec}^{-2}$ (Davidge et al. 2005; Olsen et al. 2006), is shown in Table 3. The SF of AGB stars in M31 Disk 2 falls midway between the extremes in the M83 measurements. This is consistent with the three NICI fields with the smallest R_{GC} having luminosity-weighted ages that bracket the luminosity-weighted age of the M31 disk. This does not mean necessarily that M83 and M31 have had similar star forming histories; rather, the star-forming histories of both galaxies during intermediate epochs has lead to them having similar cumulative SFs.

5. SUMMARY AND DISCUSSION

Deep near-infrared images recorded with NICI on GS have been used to investigate the spatial distribution and photometric properties of stars in the outer regions of the nearby barred spiral galaxy M83. Five fields that together sample a total area of $\sim 10^3 \text{ arcsec}^2$ (0.6 kpc^2 at the distance of M83), were observed. The fields are centered on bright NGSs, and sample large galactocentric radii. The GSC06726–0126 and 0181 fields contain a mix of stars

from the classical disk and outer disk of M83, while the stellar content of the outer disk is charted in a more pristine way with the GSC06726–0067, 0259, and 0266 fields.

Studies of the resolved stellar content of a system provide a direct check of conclusions drawn from the analysis of integrated light. A general result of the current investigation is that the ages and spatial distributions of the brightest resolved stars in the outer disk of M83 are consistent with the properties of the integrated UV light. First, the presence of bright AGB stars in all of the fields indicates that the outer disk of M83 contains a wide-spread stellar component that formed ≥ 0.2 Gyr in the past, in agreement with the luminosity-weighted age inferred from the integrated UV colors of the diffuse light around M83 and of star clusters in the outer disk. It is further worth noting that roughly half of the clusters investigated by Dong et al. (2008) using integrated IR light in the outer disk of M83 have ages > 0.2 Gyr, with the oldest having ages > 1 Gyr. The presence of AGB stars in the NICI data that span a wide range of photometric properties is consistent with such an age dispersion in the outer regions of M83.

Second, the NICI data indicate that there is an age gradient in the outer regions of M83. Based on a comparison of LFs with models, the AGB stars in the GSC06726–0126 and 0181 fields are older on average than in the fields with larger R_{GC} . The FUV – NUV color in the outer regions of M83 varies with radius (Thilker et al. 2005), in a manner that is consistent with an age gradient similar to that measured from the AGB stars.

Third, the number density of stars with $K < 22.5$ ($M_K > -6$) is constant with radius between $R_{GC} = 10$ and 13 kpc, with a projected density of 0.2 stars arcsec^{-2} (340 stars kpc^{-2}). The density of AGB stars in the GSC06726–0067 field, which is at $R_{GC} = 14.5$ kpc, is markedly lower than at smaller radii. The flat density distribution of individual stars at intermediate radii followed by a drop at larger radii is consistent with the integrated UV light, where the light profile flattens near 10 kpc before dropping at larger radii (Figure 5 of Thilker et al. 2005).

The agreement between the properties of resolved stars and integrated UV light is gratifying, as the UV light from intermediate age systems originates predominantly from main sequence stars with masses $\geq 2M_{\odot}$, which have a lifetime ≤ 1 Gyr. The stars that are traced by the UV light thus formed at the same time as the (only very slightly) more massive progenitors of the brightest AGB stars. An obvious avenue for future work is to measure the density of bright AGB stars over a larger fraction of the outer regions of M83. If, as suggested by the NICI data, bright AGB stars follow the UV light, then the number density of bright AGB stars in the field should drop dramatically at major axis radii in excess of 8.5 arcmin.

This investigation highlights the capabilities of NICI for deep photometric studies, and provides insights into the site characteristics of Cerro Pachon that relate to AO. While the design of NICI is optimized to address the challenges encountered in high contrast imaging, the observations presented here indicate that NICI can also be employed for deep photometric studies of faint objects over angular scales of ≈ 10 arcsec from the guide star. The angular resolution of these data approaches the diffraction limit of the telescope. While modest signatures of anisoplanaticity are seen, the impact on the photometric measurements is not large, and can be compensated for by applying a spatially variable PSF. In fact, for three of the five fields the PSF was sufficiently stable across the 14×14 arcsec² field that a spatially variable PSF was not required.

5.1. AGB Stars as Probes of the Recent Star Formation Rate

One condition for triggering star formation is that the density of cool gas be high enough to enable gravitational collapse. Observations indicate that the threshold gas density for collapse is $\sim 0.7 \times$ the Toomre stability statistic (Kennicutt 1989; Martin & Kennicutt 2001). While environments with gas densities that are typically lower than the critical value, such as the outermost regions of disks, are not expected to be sites of large-scale star formation, localized pockets of material with densities that are sufficient to trigger star formation may still occur. Accounting for such pockets in simulations of low density environments results in star-forming histories that are in better agreement with observations than models that assume a homogeneous ISM (e.g. Orban et al. 2008).

The occurrence of star-forming pockets in the peripheral regions of disks is evidently not a rare phenomenon, as star clusters with ages < 400 Myr are seen at large radii in many nearby galaxies. Such clusters are typically traced out to $2R_{25}$, leading Zaritsky & Christlein (2007) to conclude that star formation in the outer regions of disks is ‘common and long lasting’. Welikala et al. (2008) investigate the distribution of star-forming activity throughout galaxies in a range of environments. While star formation is most intense in the inner regions of galaxies, limited levels of star formation are consistently traced out to large radii, and there is only a modest radial decline in star-forming activity at large radii.

The average SSFR computed from UV emission averaged over the entirety of the outer regions of M83 is $1 \times 10^{-5} M_{\odot} \text{ year}^{-1} \text{ kpc}^{-2}$ (Bresolin et al. 2009). The five fields observed with NICI cover 10^3 arcsec², or ≈ 0.65 kpc². Therefore, if the SSFR has been fixed at $1 \times 10^{-5} M_{\odot} \text{ kpc}^{-2}$ then $8 \times 10^3 M_{\odot}$ of stars would have formed between 200 Myr and 2 Gyr in the past. Adopting a mass-to-light ratio $M/L_{bol} \sim 0.3$ (Mouhcine & Lancon 2002a), then the total luminosity of stars formed in the past 2 Gyr is $M_{bol} \sim -6.3$. Fuel consumption values

from Maraston (2005) predict that TP-AGB stars should contribute $\sim 20\%$ of the light, or a total $M_{bol} \sim -4.6$, to a system with an age of 2 Gyr. Given that TP-AGB stars have $M_{bol} \approx -5$ (Mouhcine & Lancon 2002b), which translates into $M_K \geq -7$, then the Bresolin et al. (2009) SSFR predicts at most ≈ 1 TP-AGB star in the five NICI fields. Given that there are many more bright AGB stars than this then the SSFR during intermediate epochs *in the south eastern quadrant of the outer disk of M83* must have been higher than the Bresolin et al. (2009) estimate. In other words, the south east quadrant of M83 appears to have been a region with a localized excess in star-forming activity for the past \approx Gyr when compared with the rest of the outer disk. The Bresolin et al. (2009) SSFR suggests that the density of bright AGB stars in other regions of the M83 outer disk should be markedly lower than in the south east quadrant, and this can be checked with observations of other fields throughout the outer disk of M83.

Using the integrated $8\mu\text{m}$ flux from star clusters, Dong et al. (2008) estimate that the SSFR in the outer disk of M83 has been $8.0 \times 10^{-4} M_{\odot} \text{ year}^{-1} \text{ kpc}^{-2}$. The clusters studied by Dong et al. (2008) are in the southern portion of the outer disk, with a projected distance of only a few kpc from the fields observed with NICI. This SSFR is an upper limit when applied to intercluster regions for two reasons. First, and most obviously, star clusters have stellar densities that exceed those in the field and may contain stars with lifetimes that are too short to allow them to disperse from their birthplaces before ending their evolution. Second, as Dong et al. (2008) note, emission from PAHs, which are not tracers of star-forming activity but will still contribute to the flux at $8\mu\text{m}$, will skew the SSFR to higher values.

The Dong et al. (2008) SSFR predicts that the total luminosity of stars that would have formed in the past 2 Gyr is $M_{bol} \approx -11.1$, and so $M_{bol} \approx -9.3$ would originate from TP-AGB stars. There would then be ≈ 50 stars with $M_{bol} = -5$ in all five NICI fields, whereas 100 TP-AGB stars are present. On first blush, it may appear that the Dong et al. (2008) SSFR is too low, which is contrary to the expectation that it might overestimate the SSFR. Still, if the AGB star counts near GSC06726–0126 and 0181 are excluded because of their proximity to the classical disk of M83, then the Dong et al. SSFR predicts that there should be 30 TP-AGB stars in the remaining fields, whereas 33 AGB stars are seen. There is thus good agreement with the numbers of bright AGB stars in the fields investigated with NICI if the fields that are least prone to contamination from the classical disk of M83 are considered. These numbers suggest that the SSFR estimated from clusters in the southernmost regions of M83 also applies to the nearby field. Such agreement also suggests that the characteristic timescale for cluster disruption in the outer disk of M83 is much lower than ~ 1 Gyr; otherwise, stars would stay locked in clusters and the SSFR inferred from the field would be much lower than observed.

5.2. Possible Origins of the Gas and Stars in the Outer M83 Disk

Bush et al. (2008) model the evolution of a disk that has an extended, constant density gas component. Spiral density waves create areas of high density in the outer disk that are sites of star formation. A diffuse stellar component subsequently forms as areas of active star formation propagate with azimuth. If an extended gas disk like that modelled by Bush et al. (2008) has been in place around M83 for a significant fraction of the Hubble time then an old, diffusely distributed stellar component will have formed *in situ*. That a substantial diffuse RGB component has not been detected in the three outermost fields argues that the outer gas disk around M83 has not been in place for longer than a few Gyr.

The processes that may cause the formation of structurally distinct inner and outer disk components may leave signatures in the stellar contents of disks. A downward breaking profile, such as is seen in the near-infrared integrated light profiles of M83, may be due to the reduced frequency at which the star formation threshold is breached in the outer regions of gas disks with a radially decreasing density profile (Elmegreen & Hunter 2006). Roskar et al. (2008) model the impact of star formation and dynamical processes on disk structure, and find that systems with a downward breaking stellar mass profile have an age minimum at the break location, due in part to the decrease in gas density towards larger radii. The mean age of stars in the outer disks of these models increases towards larger radii due to the orbital heating of old stars by secular processes.

Stars in disks may migrate over substantial radial distances. Sellwood & Binney (2002) find that stars that formed at intermediate radii in disks may be perturbed by spiral waves and move out to more than twice their radius of formation. The bombardment of the outer disk of M83 by halo sub-structures, which is a process that has been suggested as a means of explaining the kinematic characteristics of PNe in M83 (Herrmann et al. 2009), may also contribute to mixing in the M83 disk. The flat radial distribution of bright AGB stars in the four innermost NICI fields suggests that they were not scattered to large radii from the inner regions of the disk by interactions with spiral structure.

The plateau in AGB number counts that is defined by all of the NICI fields save that around GSC06726–0067 is reminiscent of an anti-truncated light profile. Such profiles may be the result of the accretion of material with an angular momentum distribution that is systematically different from that of the main body of the disk (van der Kruit 2007), dynamical evolution spurred by galaxy-galaxy interactions (e.g. Younger et al. 2007), and/or dynamical processes that stir the outer regions of disks (de Jong et al. 2007). Younger et al. (2008) find that the re-distribution of gas and stars resulting from the transfer of angular momentum in interactions may produce anti-truncated light profiles. Simulations discussed by Younger et al. (2008) predict that older stars are re-distributed to larger radii, in response

to the transfer of angular momentum as gas is channeled inwards. The stellar content of the outer disk is thus skewed to an older luminosity-weighted age than was in place prior to the interaction. Of course, not all of the gas in a disk may be channeled into the galaxy center, and if some gas is moved to large radii by tidal forces, or is stripped from one galaxy and settles in the disk plane of the other then it may eventually be an area of star formation, thereby producing an extended young stellar component, such as is seen in M83.

Erwin, Beckman, & Pohlen (2005) find that some galaxies with anti-truncated light profiles show signatures of tidal interactions, suggesting that galaxy-galaxy interactions may be related to the formation of anti-truncated systems. It has been suggested that the elevated star forming activity in M83 may have been triggered by an interaction with NGC 5253 (van den Bergh 1980, but see also Rogstad et al. 1974), or KK 208 (Karachentsev et al. 2002). Bresolin et al. (2009) conclude that a tidal origin for the outer disk of M83 can not be ruled out.

There are indications that M83 has been subjected to tidal interactions. The HI distribution in M83 is asymmetric, with $1.4\times$ more HI on the eastern side of the galaxy than the western side (Huchtmeier & Bohnenstegel 1981). The outer gas disk is also warped (e.g. Rogstad et al. 1974), a phenomenon that has been attributed to interactions with satellites in other systems (e.g. Hunter & Toomre 1969). Diaz et al. (2006) find a mass concentration in the central regions of M83 that may be the remnants of a companion that was accreted by M83. The kinematics of HI clouds seen in the vicinity of M83 are also consistent with a possible tidal origin (Miller et al. 2009). The absence of a metallicity gradient in the outer disk of M83 (Bresolin et al. 2009) suggests that this material is well-mixed, as might be expected if it has been churned by tidal forces, although Bresolin et al. (2009) point out that a homogeneous metallicity distribution may simply be a consequence of the low surface density of gas, much like that seen in dwarf galaxies. Models of disks that are subject to the infall of material from the surrounding halo can also produce flat abundance profiles at large radii (e.g. Magrini et al. 2009). An analysis of the orbital properties of the galaxies near M83 will help to determine when M83 was last subjected to a significant interaction, and if this event can be associated with the epoch of elevated star formation in its outer disk.

It is a pleasure to thank the NICI support scientist, Thomas Hayward, for invaluable advice and assistance in defining the observations and recording these data. Thanks are also extended to the anonymous referee, who made suggestions that improved the final paper.

REFERENCES

- Aguerri, J. A. L., Balcells, M., & Peletier, R. F. 2001, *A&A*, 367, 428
- Artigau, E., et al. 2008, *Proc. SPIE*, 7014, 66
- Barker, M. K., & Sarajedini, A. 2008, *MNRAS*, 390, 863
- Bakos, J., Trujillo, I., & Pohlen, M. 2008, *ApJ*, 683, L103
- Bell, E. F., & de Jong, R. S. 2000, *MNRAS*, 312, 497
- Bessell, M. S., & Brett, J. M. 1988, *PASP*, 100, 1134
- Bohlin, R. C., Cornett, R. H., Hill, J. K., Smith, A. M., & Stecher, T. P. 1983, *ApJ*, 274, L53
- Boissier, S., et al. 2005, *ApJ*, 619, L83
- Bresolin, F., Ryan-Weber, E., Kennicutt, R. C., & Goddard, Q. 2009, *ApJ*, 695, 580
- Buat, V., et al. 2008, *A&A*, 483, 107
- Crocker, D. A., & Rood, R. T. 1984, in *IAU Symp 105, Observational Tests of the Stellar Evolution Theory*, ed. A. Maeder & A. Renzini (Dordrecht: Reidel), 159
- Crosthwaite, L. P., Turner, J. L., Buchholz, L., Ho, P. T. P., & Martin, R. N. 2002, *AJ*, 123, 1892
- Crowther, P. A., Hadfield, L. J., Schild, H., & Schmutz, W. 2004, *A&A*, 419, L17
- Cutri, R. M., et al. 2003, *2MASS All-Sky Catalogue of Point Sources* (Amherst: Univ. Massachusetts Press).
- Davidge, T. J. 2000, *PASP*, 112, 1177
- Davidge, T. J. 2003, *PASP*, 115, 635
- Davidge, T. J. 2006, *ApJ*, 641, 822
- Davidge, T. J. 2007, *ApJ*, 664, 820
- Davidge, T. J. 2008, *AJ*, 136, 2502
- Davidge, T. J. 2009, *ApJ*, 697, 1439
- Davidge, T. J. 2010, *AJ*, 139, 680
- Davidge, T. J., & Courteau, S. 1999, *AJ*, 117, 1297
- Davidge, T. J., & Jensen, J. B. 2007, *AJ*, 133, 576
- Davidge, T. J., Olsen, K. A. G., Blum, R., Stephens, A. W., & Rigaut, F. 2005, *AJ*, 129, 201

- Davidge, T. J., Stoesz, J., Rigaut, F., Veran, J-P, & Herriot, G. 2004, *PASP*, 116, 1
- de Jong, R. S. et al. 2007, *ApJ*, 667, L49
- Diaz, R. J., Dottori, H., Agüero, M. P., Mediavilla, E., Rodrigues, I., & Mast, D. 2006, *ApJ*, 652, 1122
- Dong, H., Calzetti, D., Regan, M., Thilker, D., Bianchi, L., Meuer, G. R., & Walter, F. 2008, *AJ*, 136, 479
- D’Onghia, E., Burkert, A., Murante, G., & Khochfar, S. 2006, *MNRAS*, 372, 1525
- Elmegreen, B. G., & Hunter, D. A. 2006, *ApJ*, 636, 712
- Erwin, P., Beckman, J. E., & Pohlen, M. 2005, *ApJ*, 626, L81
- Ferraro, F. R., Montegriffo, P., Origlia, L., Fusi Pecci, F. 2000, *AJ*, 119, 1282
- Girardi, L., Bertelli, G., Bressan, A., Chiosi, C., Groenewegen, M. A. T., Marigo, P., Salasnich, B., & Weiss, A. 2002, *A&A*, 391, 195
- Hadfield, L. J., Crowther, P. A., Schild, H., & Schmutz, W. 2005, *A&A*, 439, 265
- Hammer, F., Flores, H., Elbaz, D., Zheng, X. Z., Liang, Y. C., & Cesarsky, C. 2005, *A&A*, 430, 115
- Hammer, F., Puech, M., Chemin, L., Flores, H., & Lehnert, M. D. 2007, *ApJ*, 662, 322
- Harris, J., & Zaritsky, D. 2001, *ApJS*, 136, 25
- Hayashi, H., & Chiba, M. 2006, *PASJ*, 58, 835
- Herrmann, K. A., Ciardullo, R., & Sigurdsson, S. 2009, *ApJ*, 693, L19
- Huchtmeier, W. K., & Bohnenstengel, H-D 1981, *A&A*, 100, 72
- Hunter, C., & Toomre, A. 1969, *ApJ*, 155, 747
- Jarrett, T. H., Chester, T., Cutri, R., Schneider, S. E., & Huchra, J. P. 2003, *AJ*, 125, 525
- Jensen, E. B., Talbot, R. J. Jr., & Dufour, R. J. 1981, *ApJ*, 243, 716
- Johnston, K. V., Hernquist, L., & Bolte, M. 1996, *ApJ*, 465, 278
- Karachentsev, I. D. et al. 2002, *A&A*, 385, 21
- Karachentsev, I. D. et al. 2007, *AJ*, 133, 504
- Kennicutt, R. C. Jr. 1989, *ApJ*, 344, 685
- Magrini, L., Sestito, P., Randich, S., & Galli, D. 2009, *A&A*, 494, 95
- Maraston, C. 2005, *MNRAS*, 362, 799
- Martin, C. L., & Kennicutt, R. C. Jr. 2001, *ApJ*, 555, 301

- Miller, E. D., Bergman, J. N., & Wakker, B. P. 2009, *ApJ*, 692, 470
- Mouhcine, M., & Lancon, A. 2002a, *A&A*, 402, 425
- Mouhcine, M., & Lancon, A. 2002b, *A&A*, 393, 149
- Nikolaev, S. & Weinberg, M. D. 2000, *ApJ*, 542, 804
- Olsen, K. A. G., Blum, R. D., Stephens, A. W., Davidge, T. J., Massey, P., Strom, S. E., & Rigaut, F. 2006, *AJ*, 132, 271
- Orban, C., Gnedin, O. Y., Weisz, D. R., Skillman, E. D., Dolphin, A. E., & Holtzman, J. A. 2008, *ApJ*, 686, 1030
- Pohlen, M., & Trujillo, I. 2006, *A&A*, 454, 759
- Rogstad, D. H., Lockhart, I. A., & Wright, M. C. H. 1974, *ApJ*, 193, 309
- Roskar, R., Debattista, V. P., Stinson, G. S., Quinn, T. R., Kaufmann, T., & Wadsley, J. 2008, *ApJ*, 675, L65
- Scannapieco, C., Tissera, P. B., White, S. D. M., & Springel, V. 2008, *MNRAS*, 389, 1137
- Schlegel, D. J., Finkbeiner, D. P., & Davis, M. 1998, *ApJ*, 500, 525
- Sellwood, J. A., & Binney, J. J. 2002, *MNRAS*, 336, 785
- Soria, R., & Wu, K. 2002, *A&A*, 384, 99
- Stetson, P. B. 1987, *PASP*, 99, 191
- Stetson, P. B., & Harris, W. E. 1988, *AJ*, 96, 909
- Thilker, D. A. et al. 2005, *ApJ*, 619, L79
- Tilanus, R. P. J., & Allen, R. J. 1993, *A&A*, 274, 707
- Tolstoy, E., Irwin, M. J., Cole, A. A., Pasquini, L., Gilmozzi, R., & Gallagher, J. S. 2001, *MNRAS*, 327, 918
- Trujillo, I., & Aguerri, J. A. L. 2004, *MNRAS*, 355, 82
- Trujillo, I., & Pohlen, M. 2005, *ApJ*, 630, L17
- van den Bergh, S. 1980, *PASP*, 92, 122
- van den Bosch, F. C., Abel, T., Croft, R. A. C., Hernquist, L., & White, S. D. M. 2002, *ApJ*, 576, 21
- Van der Kruit, P. C. 2007, *A&A*, 466, 883
- Van der Kruit, P. C., & Searle, L. 1981, *A&A*, 95, 105
- Welikala, N., Connolly, A. J., Hopkins, A. M., Scranton, R., & Conti, A. 2008, *ApJ*, 677, 970

Williams, B. F. 2002, MNRAS, 331, 293

Wood, P. R., Bessell, M. S., & Fox, M. W. 1983, ApJ, 272, 99

Wood, P. R., Bessell, M. S., & Paltoglou, G. 1985, ApJ, 290, 477

Younger, J. D., Cox, T. J., Seth, A. C., & Hernquist, L. 2007, ApJ, 670, 269

Zaritsky, D., & Christlein, D. 2007, AJ, 134, 135

GSC #	RA (2000)	Dec (2000)	R (mag)	R_{GC} (kpc)
06726–00126	13 37 17.8	–29 55 05.8	13.3	8.8
06726–00181	13 37 14.7	–29 56 17.6	10.5	9.7
06726–00259	13 37 10.3	–29 58 10.7	11.5	11.9
06726–00266	13 36 51.5	–29 58 21.6	10.7	10.5
06726–00067	13 37 38.4	–29 53 33.4	11.0	14.5

Table 1: Guide Star Locations and R Magnitudes

GSC #	C/M
06726–00067	1.2 ± 0.6
06726–00126	0.3 ± 0.2
06726–00181	0.6 ± 0.6
06726–00259	0.5 ± 0.5
06726–00266	0.3 ± 0.2
Composite 0126, 0181	0.4 ± 0.3
Composite 0067, 0259, 0266	0.5 ± 0.3

Table 2: C/M Ratios

Field #	SF
06726–00126	860 ± 90
06726–00181	2800 ± 300
06726–00259	15600 ± 2000
06726–00266	3000 ± 400
M31 D2	1250 ± 100

Table 3: Specific Frequencies of Stars with $M_K \leq -6$

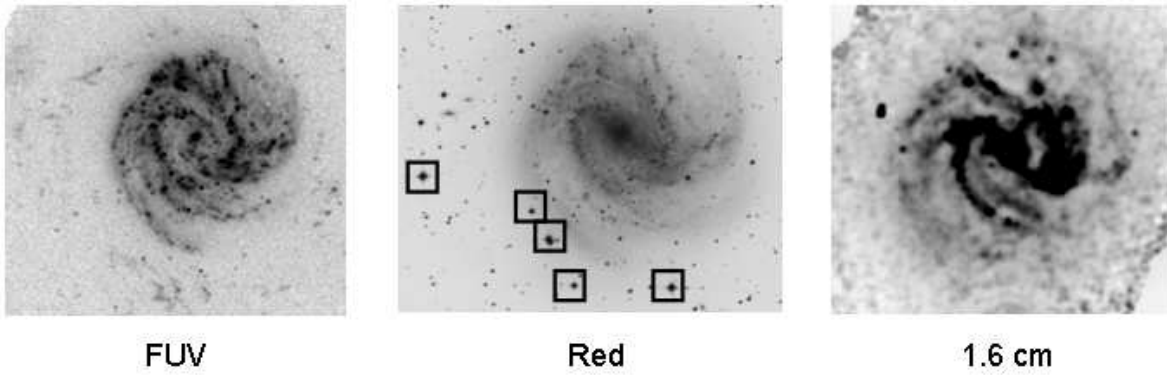


Fig. 1.— Images of M83 at three different wavelengths. The FUV GALEX image from Thilker et al. (2005), the red Digital Sky Survey image, and the 1.6 cm map from Tilanus & Allen (1993) are shown; north is at the top, and east is to the left. The images are shown with a common angular scale to facilitate comparisons, and the NICI fields are indicated on the DSS image. The actual area observed around each NGS is much smaller than the boxes used to mark the NGSs.

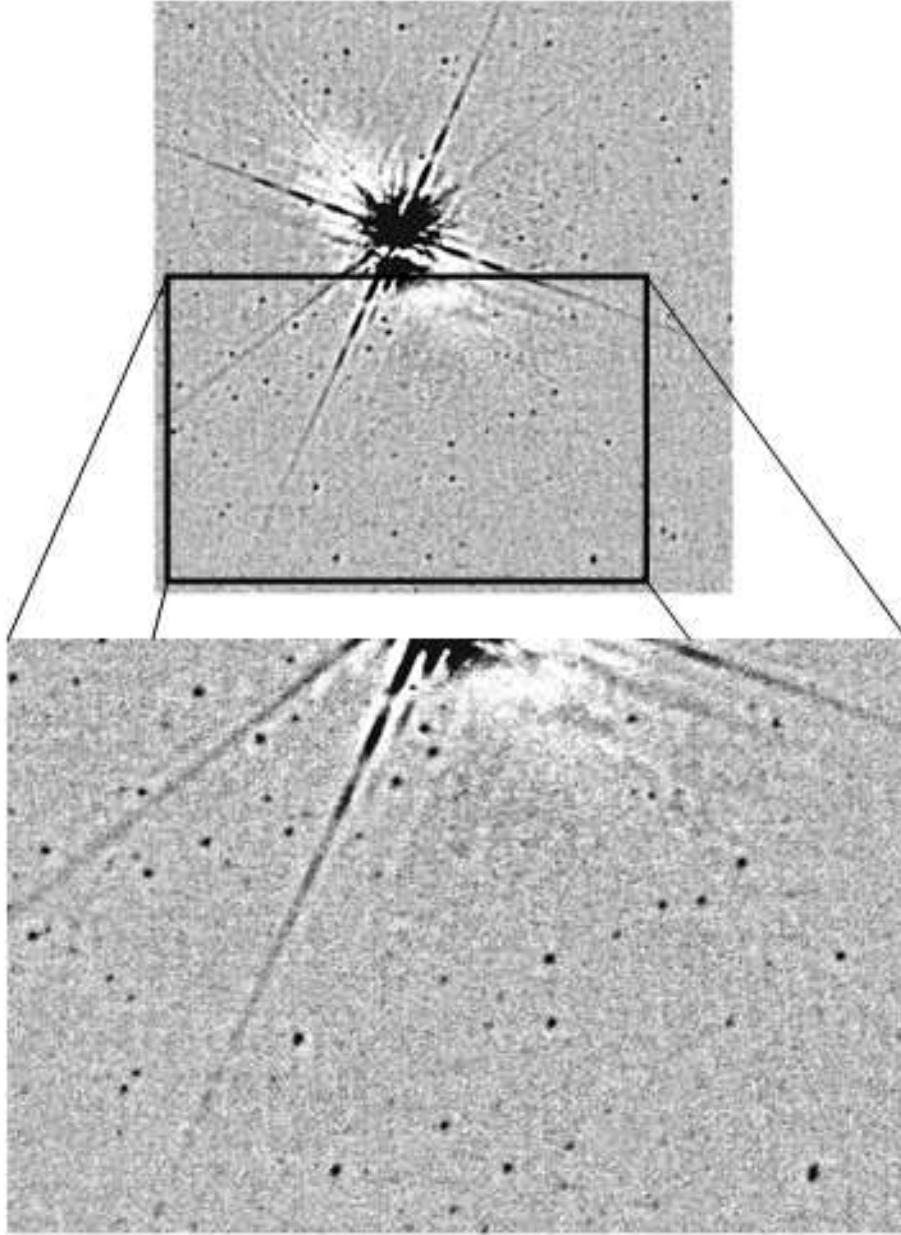


Fig. 2.— The processed H -band image of GSC 06726-00259. North is at the top, and east is to the left. The image in the top panel covers 14×14 arcsec². Speckle noise hinders the detection of faint sources near the NGS. The lower panel shows an expanded view of part of the field. Numerous sources are seen, the majority of which are AGB stars in the outer disk of M83.

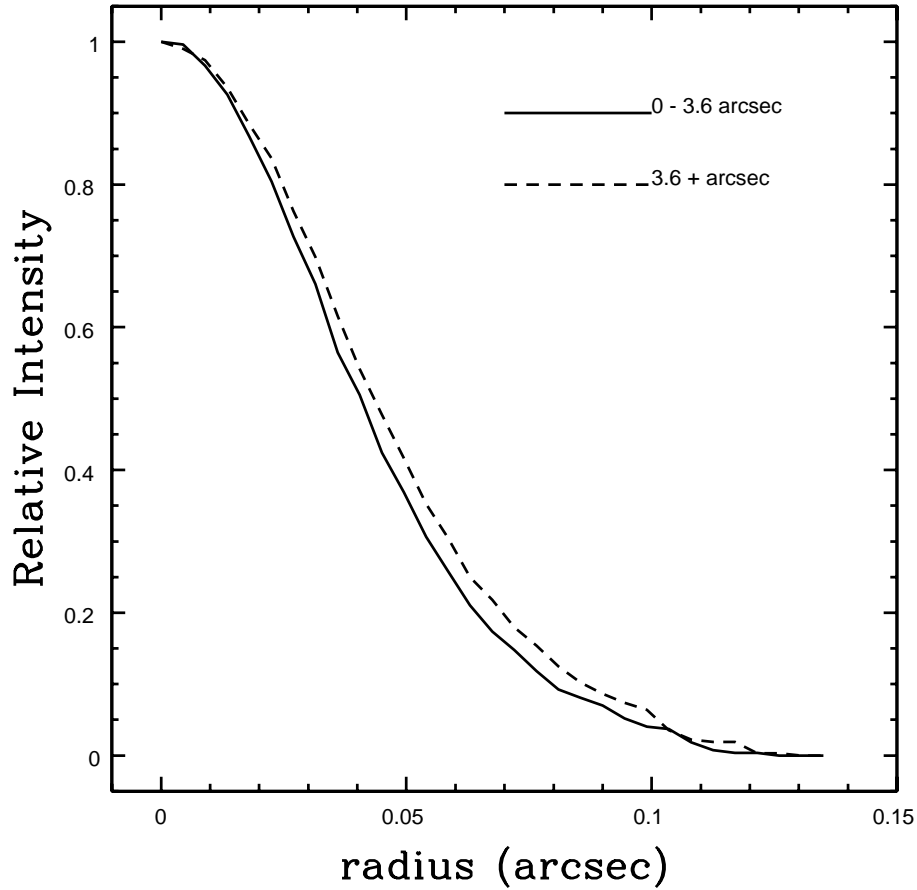


Fig. 3.— Azimuthally averaged H -band PSF profiles as constructed from sources with $r_{NGS} < 3.6$ arcsec (solid line), and $r_{NGS} > 3.6$ arcsec (dashed line), where r_{NGS} is the angular offset from GSC06726–00259. Both PSFs have been normalized to their peak intensities. The FWHMs of the two PSFs are 0.080 arcsec and 0.086 arcsec.

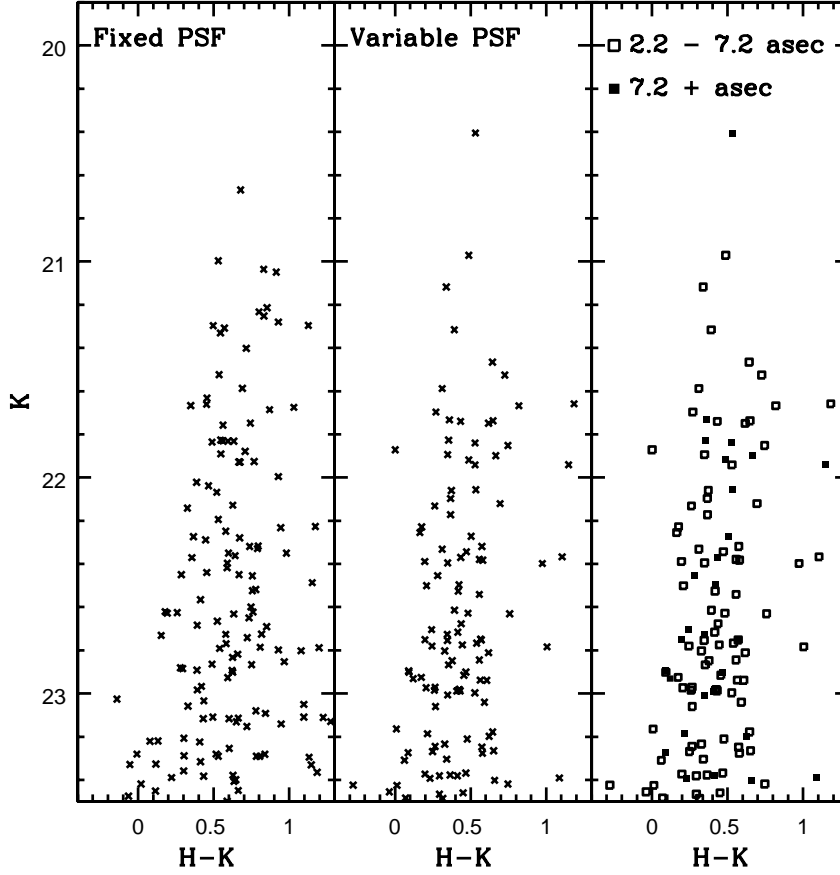


Fig. 4.— $(K, H-K)$ CMDs of the GSC06726–0259 field that were obtained by applying fixed (left hand panel) and spatially variable (middle panel) PSFs. The photometric measurements made with a variable PSF results in a tighter sequence than those made with a fixed PSF. This is one of only two fields (the other is GSC06726–0266) in which a variable PSF yields a tighter photometric sequence than a fixed PSF. The right hand panel shows the data plotted in the middle panel, but with the points identified based on r_{NGS} . Neither the ridgelines or scatter envelopes of the sequences defined by stars in the two r_{NGS} ranges differ, indicating that spatial variations in the PSF do not contribute substantial systematic photometric errors. This indicates that DAOPHOT has tracked PSF variations to a level where residual errors in the variations are modest when compared with those due to random noise (§3.1).

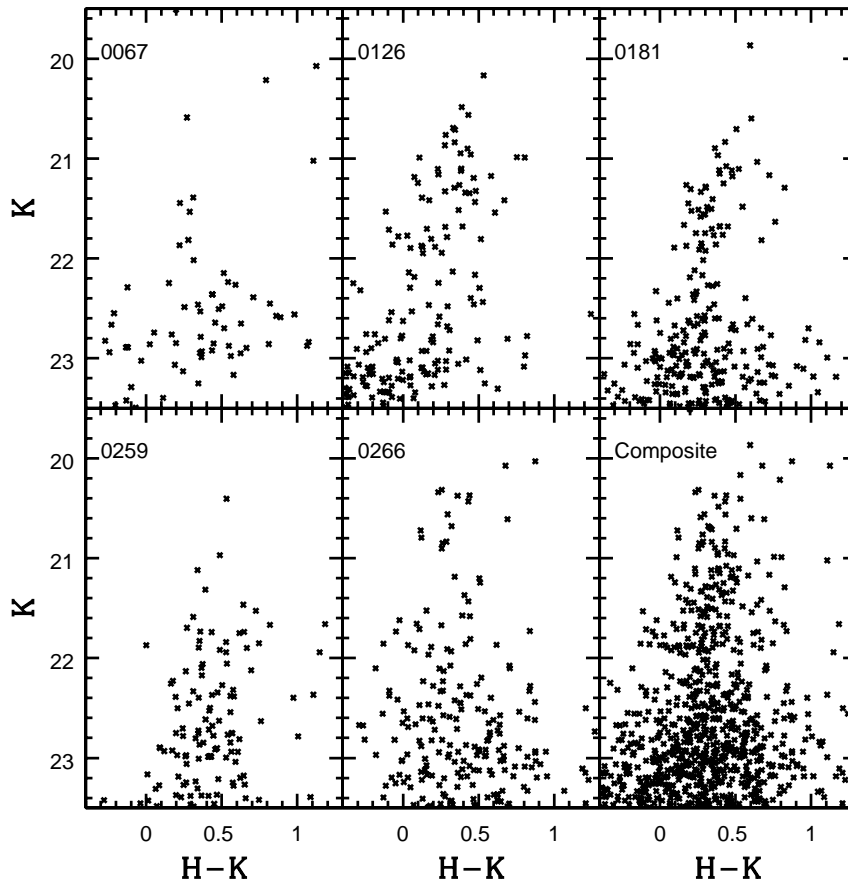


Fig. 5.— The $(K, H - K)$ CMDs of the individual fields, and the composite CMD of all fields. The bright sequence centered near $H - K \approx 0.4$ is dominated by AGB stars, although some RSGs are probably also present (§3.1.4). If an old moderately metal-rich population is present then the RGB-tip will occur near $K \approx 22$. Note that the GSC06726–0126 and 0181 CMDs differ from those of the others near the bright end, in that the AGB sequence departs from vertical. Because they are viewed close to the south east spiral arm, these fields are expected to have the greatest amount of contamination from stars in the classical disk of M83.

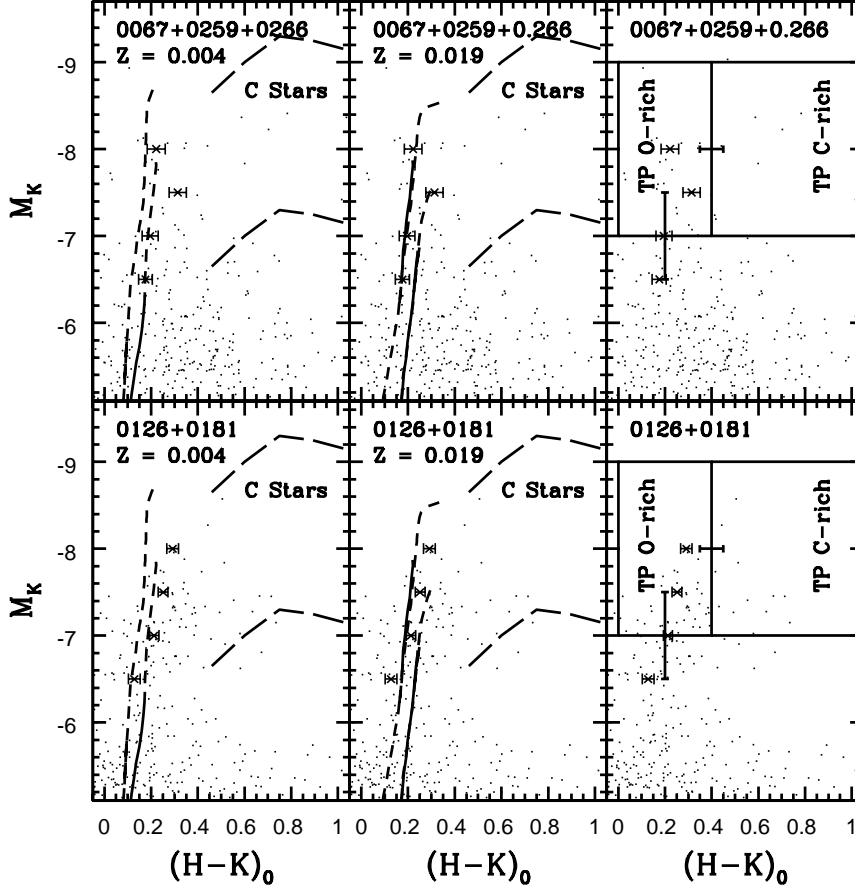


Fig. 6.— Composite CMDs of the NICI fields are compared with 1 Gyr and 10 Gyr isochrones from Girardi et al. (2002). The left hand isochrone in each panel is the 1 Gyr sequence. A distance modulus of 28.6 (Karachentsev et al. 2007) and an extinction $A_V = 1.4$ (§3.1.2) have been assumed. The portions of the isochrones that cover evolution on the RGB are shown as solid lines, while the evolution on the AGB above the RGB-tip is indicated with short dashed lines. The long dashed lines mark the area of the LMC CMD that contains cool C stars, based on the C star sequence in the Nikolaev & Weinberg (2002) CMD. The mean colors in ± 0.25 magnitude intervals in K for stars with $(H - K)_0 \leq 0.45$ are also shown for each composite CMD, and the error bars show the 1σ uncertainties in these means. The stars with $M_K \geq -7.8$ have intermediate ages, and the mean $H - K$ colors of both field groupings better match the solar metallicity sequences at $M_K = -8$ than the sub-solar metallicity sequences. The areas of the CMDs used to count M giants and C stars are indicated in the right hand panel. The error bars in this panel show (1) the uncertainty in M_K that corresponds to the onset of TP evolution for M giants, and (2) the uncertainty in the $H - K$ color that separates the areas of the CMD that are dominated by M giants and C stars. at $M_K = -8$.

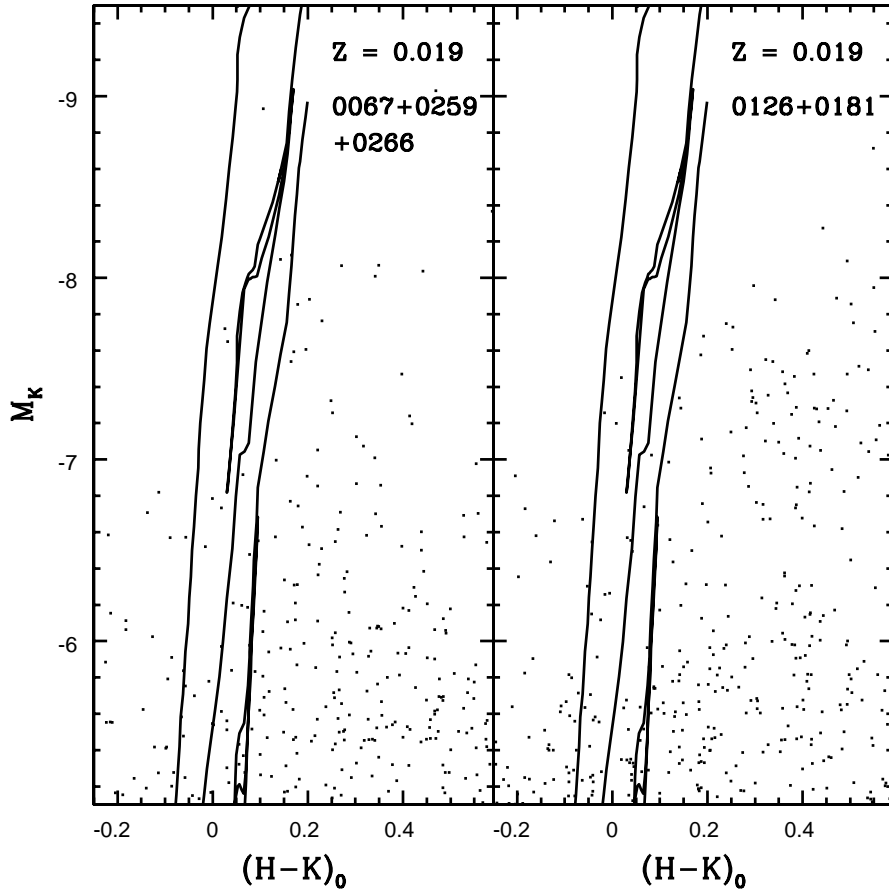


Fig. 7.— The same as Figure 6, but showing $Z = 0.019$ isochrones with ages 10 Myr, 30 Myr, and 100 Myr. Both the inner and outer disk field groupings contain stars with $(H-K)_0 < 0.2$ and $M_K < -7$ that, based on their colors, are candidate RSGs.

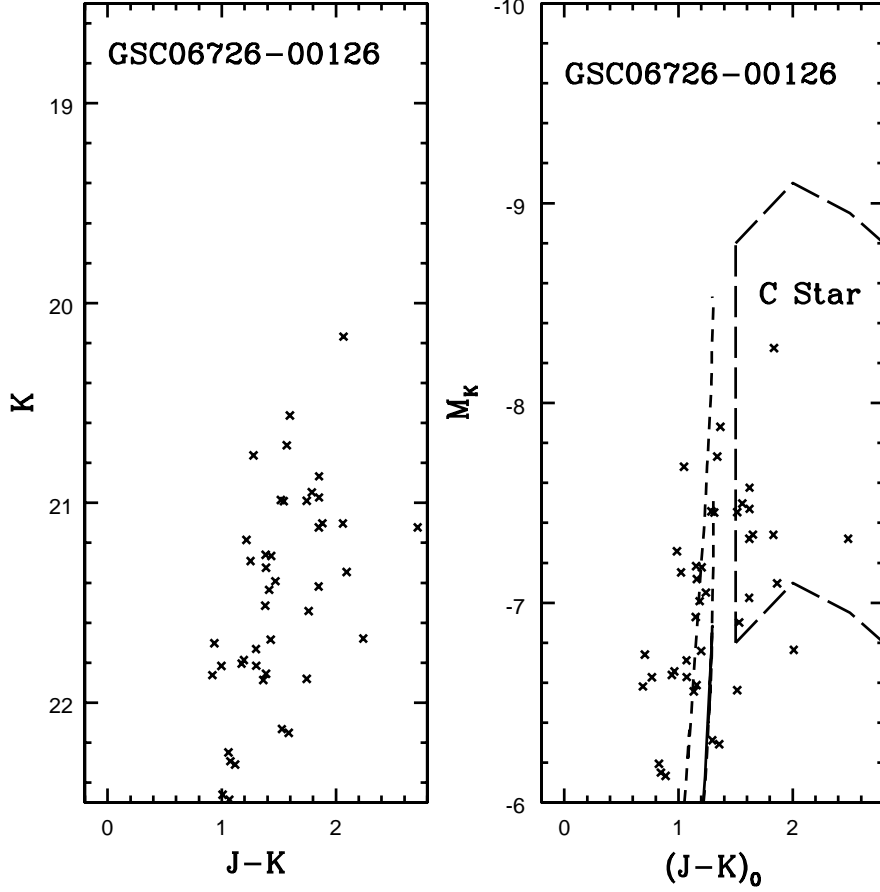


Fig. 8.— The $(K, J - K)$ and $(M_K, J - K)$ CMDs of objects near GSC06726-00126. Isochrones from Girardi et al. (2002) with ages 1 and 10 Gyr and $Z=0.019$ are shown in the right hand panel, with evolution on the RGB (solid line) and AGB (dashed line) indicated. A distance modulus of 28.6 (Karachentsev et al. 2007) is assumed, with a line-of-sight extinction $A_V = 1.4$. The photometric properties of the sources with $M_K \leq -7$ and $J - K < 1.4$ are consistent with them belonging to an intermediate age population that has an age ≈ 1 Gyr based on the peak magnitude of AGB stars. The area of the LMC $(K, J - K)$ CMD from Nikolaev & Weinberg (2000) that contains C stars is also indicated, and a number of sources have $J - K$ colors that are consistent with them being C stars.

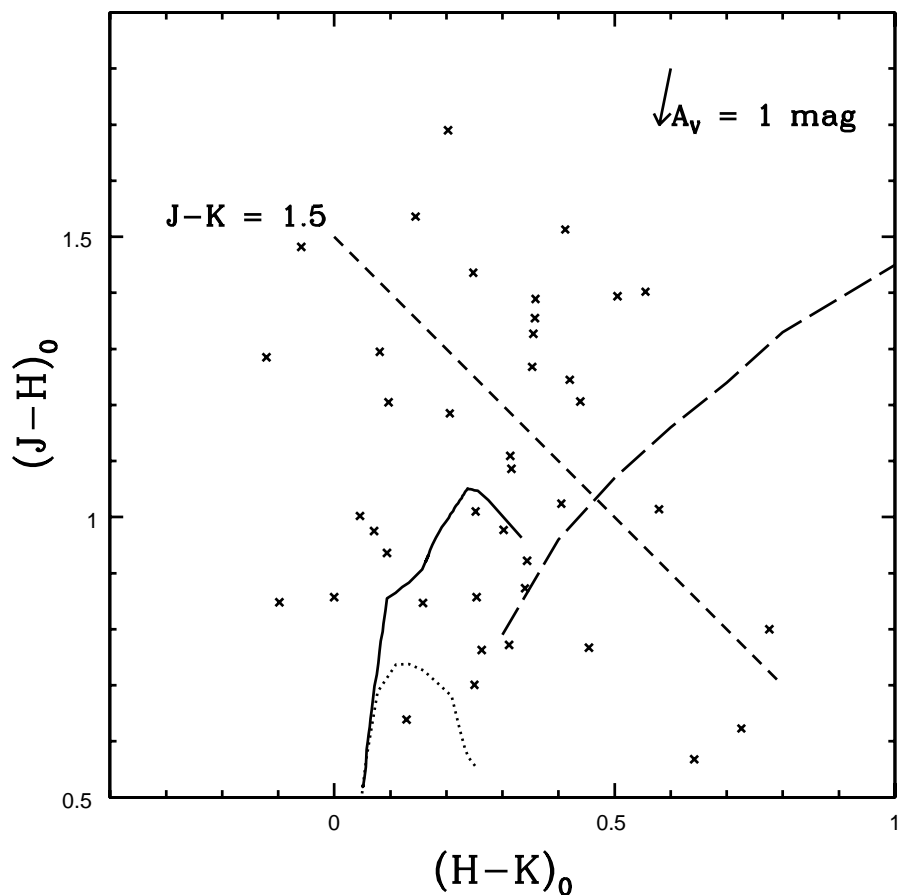


Fig. 9.— The $(H - K, J - H)$ diagram of sources near GSC06726–00126. Only objects with $K < 22$ are shown. The loci of solar neighborhood giants and dwarfs from the $Z = 0.019$ 1 Gyr isochrone from Girardi et al. (2002) are shown as solid and dotted lines, while the long dashed line shows the locus of SMC and LMC LPVs from observations tabulated by Wood et al. (1983; 1985). The line indicating $J - K = 1.5$, which is the approximate color dividing giants with oxygen-rich and carbon-rich atmospheres, is also indicated. The majority of sources with $K < 22$ have $J - H > 0.7$, and hence are not foreground main sequence stars.

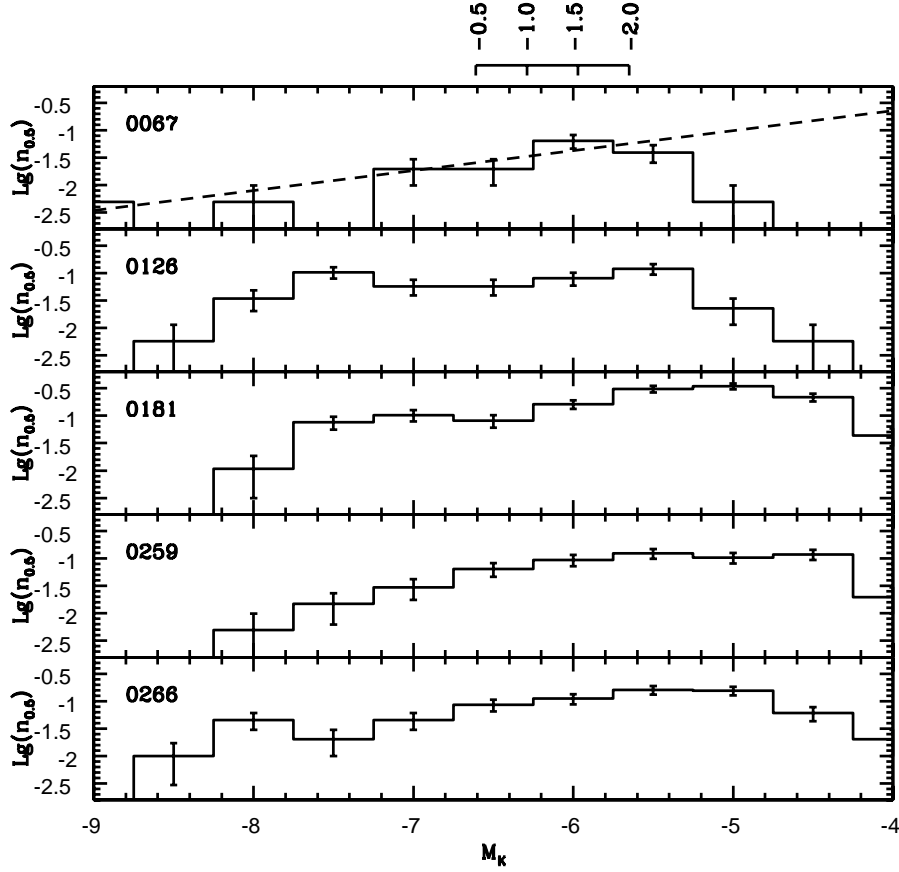


Fig. 10.— The LFs of sources with $(H - K)_0$ between -0.05 and 0.45 . $n_{0.5}$ is the number of sources arcsec^{-2} per 0.5 magnitude in K . The dashed line in the top panel is a least squares fit to the GSC06726–0067 LF, and this relation is used to estimate an upper limit to background galaxy contamination in the LFs in Figure 11. The RGB-tip brightnesses for four metallicities, based on the Galactic globular cluster calibration of Ferraro et al. (2000), are indicated at the top of the figure.

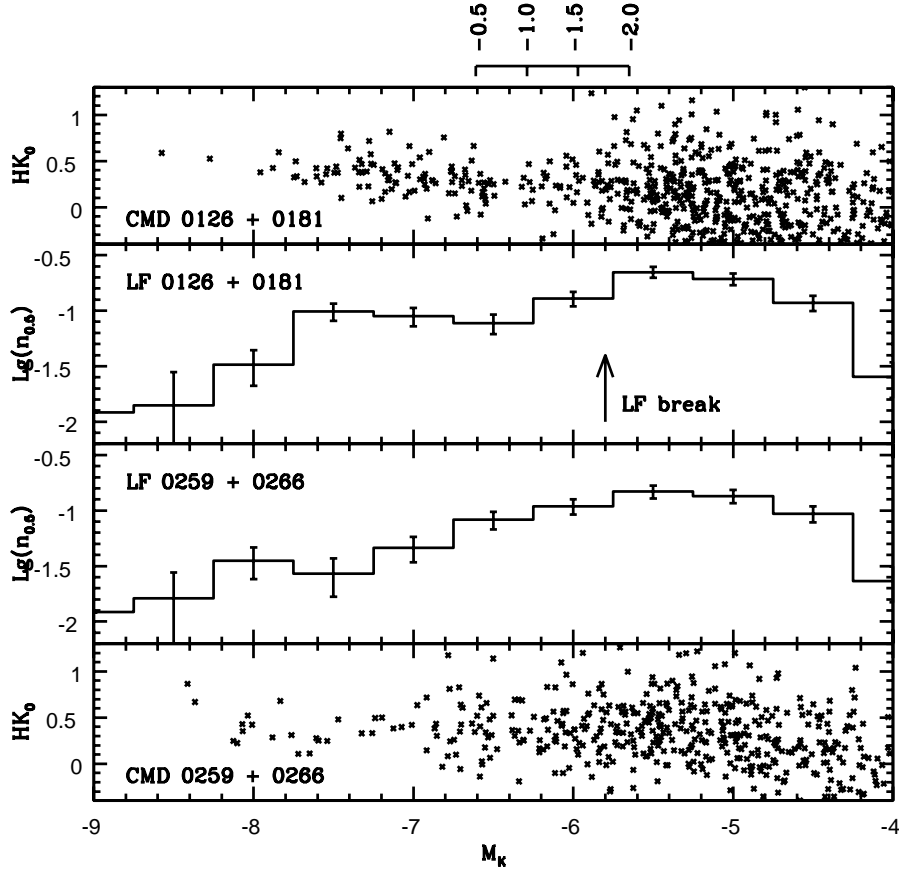


Fig. 11.— The K LFs of sources near GSC06726–0126 + 0181 and GSC06726–0259 + 0266, where $n_{0.5}$ is the number of sources arcsec $^{-2}$ per 0.5 magnitude. The dashed line in the top panel of Figure 10 was subtracted from the summed LFs to correct for contamination from background galaxies. The CMDs of GSC06726–0126 + 0181 and GSC06726–0259 + 0266 are also shown to permit features in the LFs and CMDs to be compared. The brightness of the RGB-tip for systems with various metallicities, based on the calibration of Ferraro et al. (2000), is shown at the top of the figure. The break in the mean GSC06726–0126 + 0181 LF near $M_K = -5.8$ is accompanied by a broadening of the composite CMD.

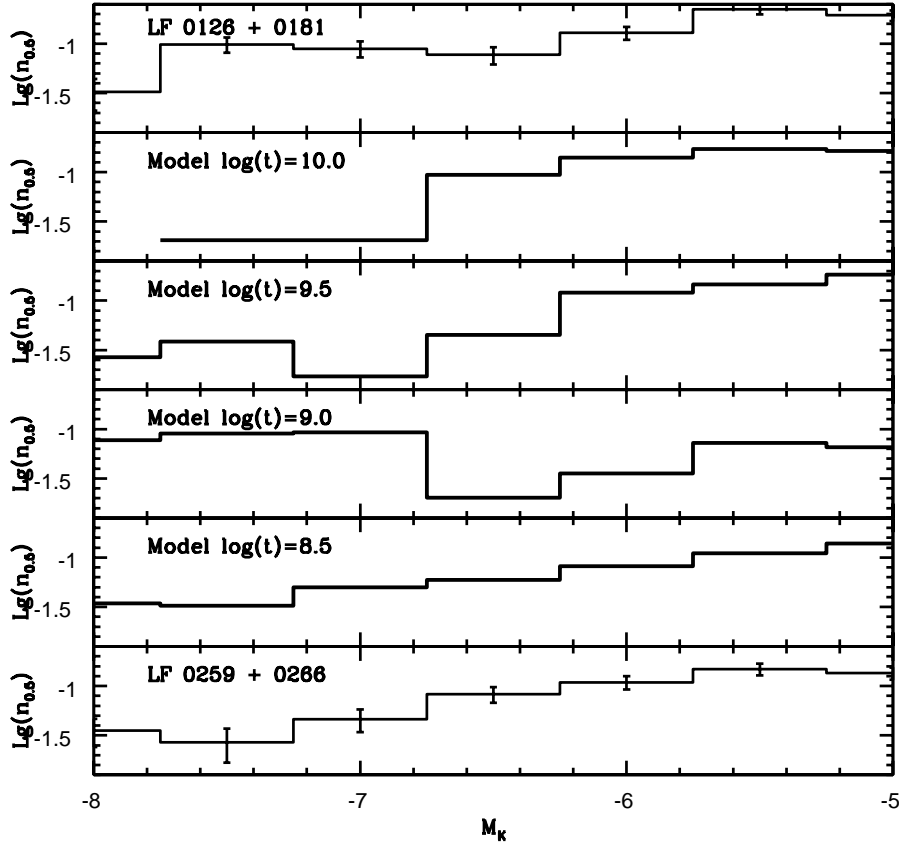


Fig. 12.— The K LFs of sources near GSC06726–0126 + 0181 and GSC06726–0259 + 0266, as shown in Figure 11. Model LFs for simple stellar populations with solar metallicities constructed from the Girardi et al. (2002) isochrones are also shown. The GSC06726–0259+0266 LF is well matched by the $\log(t) = 8.5$ LF, whereas the GSC06726–0126+0181 LF appears to be a mix of the $\log(t) = 9.0$ and older sequences.

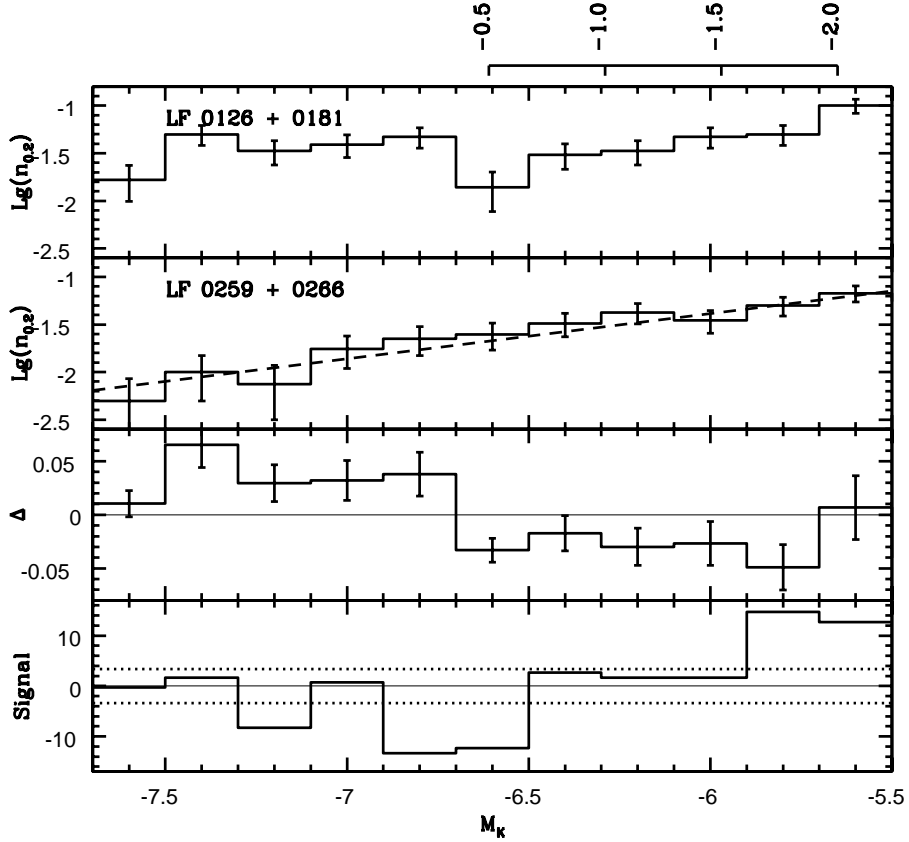


Fig. 13.— The K LFs of sources near GSC06726–0126 + 0181 and GSC06726–0259 + 0266, where $n_{0.2}$ is the number of sources arcsec^{-2} per 0.2 magnitude. The GSC06726–0259+0266 LF follows a power-law, and the dashed line in the second panel is a power-law that was fit to the LF using the method of least squares. The difference, Δ , between this power-law and the mean GSC06726–0126+0181 LF, after the latter was scaled to match the number of stars in the GSC06726–0126 and 0181 fields, is shown in the third panel. Significant residuals are seen, indicating that the power-law does not represent adequately the GSC06726–0126+0181 LF. The Sobel-convolved GSC06726–0126+0181 LF is shown in the bottom panel, and the dotted lines indicate the 1σ variance in the Sobel-convolved GSC06726–0259+0266 LF. The break at $M_K = -5.8$ in the GSC-06726–0126+0266 LF is significant at the 3.6σ level. The brightness of the RGB-tip at four metallicities, based on the empirical calibration of Ferraro et al. (2000), is shown at the top of the figure. This calibration indicates that the break corresponds to $[M/H] = -1.8 \pm 0.1$ if the RGB is dominated by old stars. This is lower than expected from a disk population, and in §3.3 it is argued that the break may not be due to the RGB-tip.

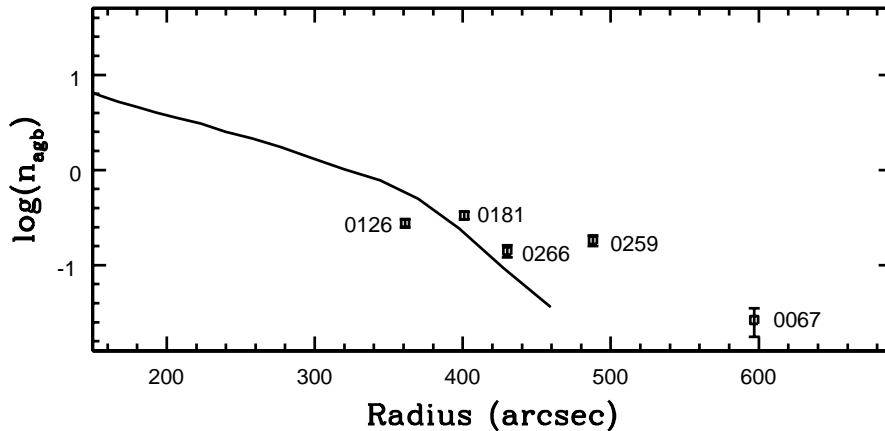


Fig. 14.— The number density of AGB stars as a function of angular separation from the center of M83 as measured in the plane of the disk. n_{agb} is the number of sources with $K \geq 22.5$ arcsec $^{-2}$, and the errorbars show the uncertainties due to counting statistics. With the exception of the field around GSC06726–0067, $n_{agb} \approx 0.2$ stars arcsec $^{-2}$. The solid line is the number density of AGB stars predicted from the K –band surface brightness profile of M83 from Jarrett et al. (2003) using the procedure described in the text. The densities of AGB stars around GSC06726–0259 and GSC06726–0067 fall well above the extrapolation of the number density curve generated from the light profile, suggesting that the fractional contribution made by AGB stars to the total light in K changes with radius.